

Designing topology and fractionalization in narrow gap semiconductor films via electrostatic engineering

Tixuan Tan,^{1,*} Aidan P. Reddy,^{2,*} Liang Fu,² and Trithep Devakul¹

¹*Department of Physics, Stanford University, Stanford, CA 94305, USA*

²*Department of Physics, Massachusetts Institute of Technology, Cambridge, Massachusetts 02139, USA*

(Dated: January 14, 2025)

We show that topological flat minibands can be engineered in a class of narrow gap semiconductor films using only an external electrostatic superlattice potential. We demonstrate that, for realistic material parameters, these bands are capable of hosting correlated topological phases such as integer and fractional quantum anomalous Hall states and composite Fermi liquid phases at zero magnetic field. Our results provide a path towards the realization of fractionalized topological states in a broad range of materials.

Introduction — Recent years have seen a great effort in the design of quantum materials with tailored electronic properties. Topological bands with tunable Chern numbers are particularly sought after because electron-electron interaction in partially filled flat Chern bands can give rise to fractional Chern insulators (FCI) [1–7] that host fractionalized quasiparticle excitations. To date, much study has been focused on two-dimensional van der Waals (vdW) heterostructures, which provide a highly versatile platform for realizing topological moiré bands [8–12]. Various graphene and semiconductor moiré superlattices host a time-reversed pair of Chern bands of opposite spin and/or valley polarization. In these systems, FCI states can form at zero magnetic field when Coulomb interaction drives spontaneous spin/valley ferromagnetism [13, 14]. In twisted bilayer MoTe₂ [15–18] and hBN-aligned pentalayer rhombohedral graphene [19], these zero-field FCI states showing fractionally quantized anomalous Hall (FQAH) effects have been experimentally observed.

Despite their remarkable tunability, moiré devices made from exfoliated 2D material flakes face challenges in terms of robustness and scalability in production [20]. In contrast, epitaxially grown semiconductor films and heterostructures have historically provided high-mobility electron gases for quantum Hall research [21]. A natural and pressing question is whether it is possible to create fractionalized electron phases in semiconductor films at zero magnetic field.

In this work, we present a general mechanism for realizing topological and fractionalized phases in thin films of narrow gap semiconductors through electrostatic engineering. We show, using a universal low-energy model, that an externally applied electrostatic superlattice potential can lead to strong hybridization of the parent conduction and valence bands, resulting in the formation of topological minibands with highly tunable bandwidth and topology. Through many-body calculations, we demonstrate that robust integer and fractionalized topological states can be realized with realistic model parameters.

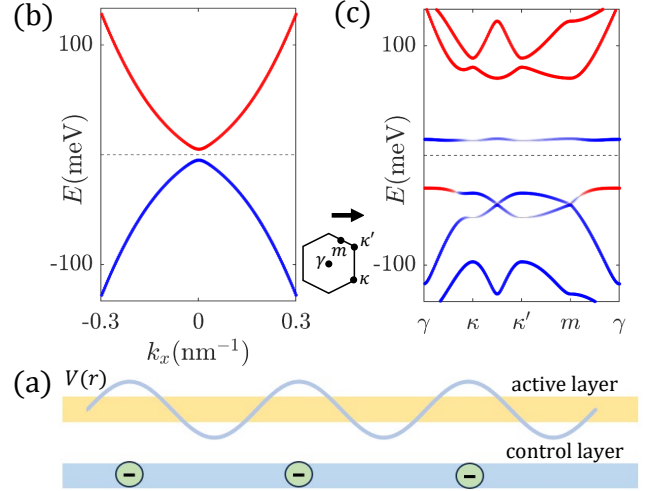


FIG. 1. Illustration of the proposed setup. (a) A control layer, hosting a periodic charge distribution, imparts an electrostatic superlattice potential on a nearby active layer composed of a narrow gap semiconductor film. (b,c) The electronic bands in the active layer is illustrated without and with the effect of the superlattice potential. For an appropriately chosen superlattice potential, topological flat bands can be achieved. Color of the bands (red and blue) indicates the orbital content of the band.

The proposed setup is illustrated in Fig 1. The “active layer” is a narrow gap semiconductor film, whose low-energy electronic structure is illustrated in Fig 1 (b). It is placed in close proximity to a “control layer”, featuring a periodic modulation of charge density with a period on the order of 10 nanometers and experimentally feasible. The periodic charge density may be realized, for instance, via a doped moiré superlattice [22–24]. The modulated charge density in the control layer produces an electrostatic superlattice potential acting on electrons/holes in the active layer, resulting in the formation of topological minibands, Fig 1(b,c). This method for realizing an electrostatic superlattice potential has been demonstrated experimentally in several available platforms [22–36]; and

* These authors contributed equally to this work.

such setups have been explored with graphene [37–41] and 2D electron gases [42, 43] as active layers.

Designing topological bands — We take as our starting point the two-band $k \cdot p$ Hamiltonian [44, 45],

$$H_0^\tau(\mathbf{k}) = \begin{pmatrix} \alpha_1 |\mathbf{k}|^2 + \frac{\delta}{2} & v(\tau k_x - i k_y) \\ v(\tau k_x + i k_y) & -\alpha_2 |\mathbf{k}|^2 - \frac{\delta}{2} \end{pmatrix} \quad (1)$$

H_0^τ describes a large class of narrow gap semiconductor films in which the conduction and valence bands have opposite parity, containing all terms up to k^2 allowed by inversion, time reversal and rotational symmetry [44, 46]. Eq 1 is written in the eigenbasis of σ_z , labeled $\{|1\rangle, |2\rangle\}$, which represents the orbitals making up the conduction and valence bands. $\tau = \pm 1$ denotes Kramers degeneracy associated with electron’s spin. The effective parameters $\delta, v, \alpha_1, \alpha_2$ are material and thickness dependent. Thus far, $H_0^\tau(\mathbf{k})$ describes the low-energy electronic properties of a pristine 2D semiconductor film.

We consider the effect of an electrostatic superlattice potential. We focus on the C_3 symmetric potential,

$$V(\mathbf{r}) = 2V_0 \sum_{n=1}^3 \cos(\mathbf{g}_n \cdot \mathbf{r} + \phi) \quad (2)$$

where $\mathbf{g}_n = g(-\cos \frac{2\pi n}{3}, \sin \frac{2\pi n}{3})$. The potential is characterized by its strength V_0 , reciprocal lattice vector $g = \frac{4\pi}{\sqrt{3}a}$ where a is the superlattice period, and the parameter ϕ which controls the shape of the potential. We fix $\phi = \pi$, which gives a superlattice potential with minima forming a triangular lattice and maxima forming a honeycomb lattice. We take $V(r)$ to couple only to the in-plane density, i.e. the coupling is proportional to identity in σ . effect of the finite thickness of the film, as well as other potential shapes ϕ , are discussed in the Supplemental material [46]. The potential $V(r)$ produces mini-bands in the mini-Brillouin zone defined by \mathbf{g} , as illustrated in Fig 1b.

At very low energy or very long wavelengths, the k^2 term in Eq 1 can be neglected ($\alpha_1, \alpha_2 \rightarrow 0$), in which case H_0^τ describes a massive Dirac fermion. In this limit, an appropriate choice of superlattice potential $V(r)$ can be used to realize topological single-particle bands [47, 48]. However, as shown in the Supplementary Material [46], we find that Coulomb interactions are unable to stabilize a spin-polarized Chern insulator at integer filling in this limit. We therefore turn to the full $k \cdot p$ Hamiltonian H_0^τ including the quadratic terms.

For simplicity, we set $\alpha_1 = \alpha_2 \equiv \alpha$. We define an energy scale $E_D = v^2/\alpha$ and momentum scale $k_D = v/\alpha$, which characterizes the energy and momentum above which the massive Dirac fermion description breaks down and the quadratic terms in H_0 becomes important. Up to these overall energy and momentum scales, the single particle physics of our model is controlled entirely by three dimensionless parameters $\delta/E_D, V_0/E_D$, and g/k_D .

We focus on the properties of the first conduction miniband of $\tau = +$ (bands of $\tau = -$ are related by time reversal symmetry). In Fig 2(a,b), we show the bandwidth

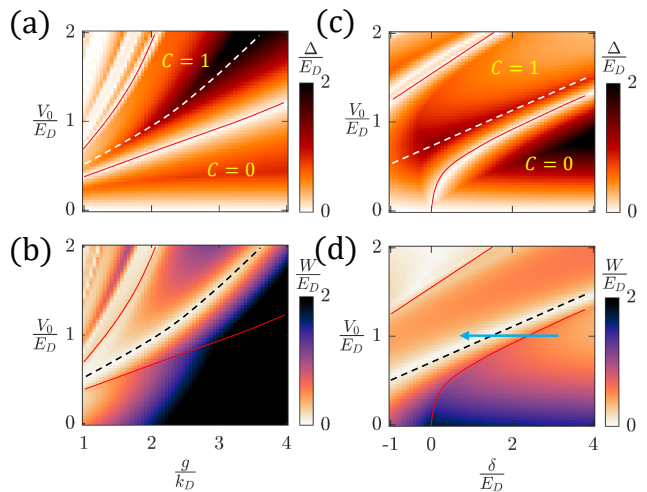


FIG. 2. Phase diagram of the model. The (a,c) direct gap Δ , (b,d) bandwidth W of the first conduction miniband as a function of superlattice potential strength V_0 , reciprocal wave vector g , and pristine gap δ . (a,b) is plotted at $\frac{\delta}{E_D} = 1$, and (c,d) is plotted at $\frac{g}{k_D} = 2$. The solid lines delineates the boundary of topological $C = 1$ phase, and the dashed line indicates where the bandwidth is minimized. The blue arrow in (d) is discussed in the main text.

(W) and minimum direct gap (Δ) as a function of the dimensionless superlattice potential parameters V_0/E_D and g/k_D , for a fixed $\delta/E_D = 1$. We highlight a robust $C = 1$ region spanning a wide parameter range. Importantly, topological minibands are formed even when the pristine semiconductor films have topologically trivial band structure ($\delta > 0$). In a large portion of this region, $W \ll \Delta$, implying that Coulomb interactions are likely to result in a spin polarized quantum anomalous Hall (QAH) insulator at filling $n = 1$ electron per superlattice unit cell – a scenario we will soon confirm.

Within this region, we further find an optimal line (indicated by the dashed line) along which the band becomes almost perfectly flat. This flat band is nearly “ideal” for the realization of fractionalized topological phases at partial fillings [49–55], and is similar to those previously found in certain moiré materials [10, 56–61] (we discuss various quantum geometric indicators in the Supplemental material [46]). In Fig 2(c,d) we show the same quantities, but as a function of V_0/E_D and δ/E_D , for a fixed value of $g/k_D = 2$. We again find a robust $C = 1$ phase accompanied by a line of almost vanishing bandwidth. Collectively, our findings imply that the topological $C = 1$ phase, with $W \ll \Delta$, is robust over a wide region of the three-dimensional parameter space, and that the bandwidth nearly vanishes along an optimal two-dimensional surface in this space.

To understand the emergence of the topological flat band, we consider tuning δ while keeping all other parameters fixed. First, consider the limit of large $\delta \rightarrow \infty$, in which the conduction band (from orbital $|1\rangle$) and valence

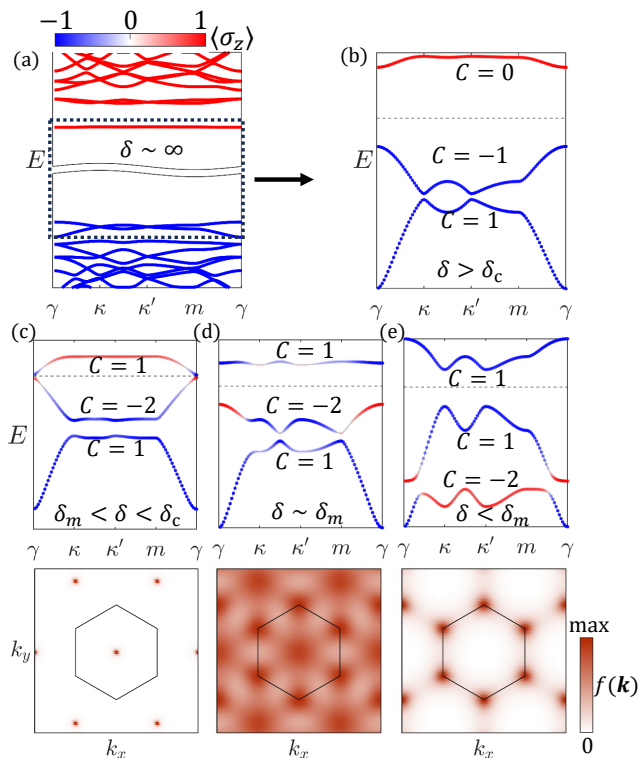


FIG. 3. Illustration of the first minibands as δ is tuned. The color indicates the $\langle \sigma_z \rangle$ expectation value. The Chern numbers of each miniband are labeled. We show (a) the large δ limit, (b) $\delta > \delta_c$ before inversion, (c) $\delta_m < \delta < \delta_c$ immediately after inversion, (d) $\delta = \delta_m$ at the magic value, and (e) $\delta < \delta_m$ below the magic value. Bottom panels of (c,d,e) show the corresponding Berry curvature $f(\mathbf{k})$ of the first conduction miniband, with boundary of mBZ indicated by the black solid line. The bandwidth is minimized and the Berry curvature distribution is most uniform near δ_m .

band (from orbital $|2\rangle$) of H_0^c are separated in energy and essentially unhybridized. As illustrated in Fig 3a, in the presence of the superlattice potential $V(r)$, the first (lowest-energy) $|1\rangle$ miniband resembles that of a triangular lattice tight binding model centered at the potential minima; while the first two (highest-energy) valence minibands from $|2\rangle$ resembles those of a honeycomb lattice centered at the potential maxima. At large but finite δ , Fig 3b, the mini-Dirac points at κ and κ' in the $|2\rangle$ bands are gapped out by an effective Haldane type term, generated by virtual tunneling processes with the $|1\rangle$ band, resulting in topological bands.

We now consider reducing δ , along the trajectory marked by the blue arrow in Fig 2d. There are two notable points: a critical δ_c at which the gap closes, and a “magic” δ_m at which the bandwidth is minimized, corresponding to the solid and dashed lines.

The emergence of the nearly flat band can be understood by considering δ slightly above and below δ_m . At $\delta = \delta_c > \delta_m$, the first conduction and valence minibands undergo a topological band inversion at γ , resulting in

a topological first conduction band with an energy minimum at γ , shown in Fig 3c. When $\delta < \delta_m$, Fig 3e, this band evolves smoothly into an upper honeycomb band of majority $|2\rangle$ character, with energy minima at κ and κ' . The magic δ_m , Fig 3d, occurs between these two limits: the energy dispersion is suppressed as the energy extrema swap positions in the Brillouin zone.

Beyond just bandwidth, the Berry curvature $f(\mathbf{k})$ also becomes extremely uniform near δ_m . Immediately following the mini-band inversion, $\delta \approx \delta_c > \delta_m$ (Fig 3c), Berry curvature concentrates near the inversion point γ . In contrast, when $\delta < \delta_m$ (Fig 3e), the band’s honeycomb character leads to Berry curvature hotspots at κ, κ' . Near the crossover $\delta \sim \delta_m$ between these extremes (Fig 3d), Berry curvature fluctuations are suppressed. Additionally, due to the crossover from triangular to honeycomb-like bands, the charge density in real space also becomes evenly distributed near δ_m [46].

We remark that this crossover is highly reminiscent of a similar mechanism leading to nearly ideal flat bands in twisted TMD homobilayers [57, 59, 62], a platform in which FQAH has been observed experimentally [15–18]. Similar flat bands have also been observed in the context of quasiperiodicity [63, 64]. Finally, although we have considered tuning δ to make the physical origin of the flat bands clear, any other parameter can also be used to tune to the flat band.

Example — As an example of our theory, we consider Cd_3As_2 . In bulk form, Cd_3As_2 is a 3D Dirac semimetal [65–71]. In films, it oscillates between a 2D trivial or topological insulator [65, 72] depending on thickness, in good agreement with low-energy $k \cdot p$ modeling [65, 73–75]. Fig. 4(a) shows the parent bandgap $|\delta|$ (that is, the bandgap in the absence of a superlattice potential) of Cd_3As_2 thin film as a function of its thickness L obtained by solving the 3D $k \cdot p$ model [73] in the thin film geometry [46]. The film is a non-trivial 2D Z_2 topological insulator for $10 \text{ nm} \lesssim L \lesssim 19 \text{ nm}$.

To identify optimal film thicknesses for realizing topological flat minibands by our mechanism, we observe from Fig 2(c,d) that the bandwidth-to-bandgap ratio is most optimal when δ is small and positive. This suggests that one should choose L to be close to a topological band inversion, on the trivial side. Based on this criterion and Fig. 4(a), we take $L = 8 \text{ nm}$. We remark that this criterion may be useful as an experimental “shortcut” to identifying optimal film thicknesses even in the absence of knowledge of full microscopic band structure.

We derive an effective two-band $k \cdot p$ Hamiltonian for 8 nm Cd_3As_2 thin film of the form of Eq 1 with parameters listed in Fig 4 [46]. Note that because $\alpha_1 \neq \alpha_2$, this model is particle-hole asymmetric and does not map exactly to Fig 2. Nevertheless, we still expect the topological flat band based on our physical picture for their origin. As the valence band is significantly more massive ($\alpha_2 \ll \alpha_1$), we consider the first valence miniband in the presence of an electrostatic potential of the form Eq. 2 with $\phi = 0$ and a realistic superlattice period $a = 20 \text{ nm}$.

For a range of V_0 , the first valence miniband becomes topological ($C = \pm 1$), flat, and well isolated as shown in Fig. 4(b).

Many-body analysis — Having established the existence of flat Chern bands, we now demonstrate their potential for realizing topological and fractionalized phases via a fully interacting many-body analysis. Here, we focus the first valence miniband of Cd_3As_2 thin films as introduced above. We define the filling factor n as the number of holes per superlattice unit cell relative to charge neutrality. Focusing on the filling range $0 < n \leq 1$, we introduce a two-body Coulomb interaction $V_C(r) = \frac{e^2}{\epsilon|r|}$ between holes and perform exact diagonalization within the Hilbert subspace of the time-reversed pair of first valence minibands. Finally, we define the total spin $S_z = \frac{1}{2}(N_+ - N_-)$, where N_τ is the number of electrons in the τ Chern band, which is a conserved quantum number.

In Fig. 4(c), we show the magnon gap Δ_s at $n = 1$, defined as the energy difference between the lowest-energy states in the fully polarized $S_z = S_z^{\text{max}}$ sector and the $S_z = S_z^{\text{max}} - 1$ sector. We find that, throughout a range of V_0 , $\Delta_s > 0$ indicating a fully spin-polarized Chern insulator ground state [46]. This robust integer QAH effect can be attributed to flat band ferromagnetism, arising due to the topological band with $W \ll \Delta$.

Next, we examine fractional fillings $n = \frac{1}{3}$ and $\frac{2}{3}$. Fig. 4 (d) and (e) demonstrate the evolution of the low energy spectra within the fully spin-polarized sector at $n = \frac{1}{3}, \frac{2}{3}$ with varying V_0 . The large gap between the fourth and third lowest energy states marked by the red and blue lines, indicates a gapped, three-fold quasi-degenerate ground state. By examining their center-of-mass momenta, we confirm that these ground states are fractional Chern insulators, as opposed to a charge density waves with tripled unit cells [46, 60, 62, 76, 77]. We have verified on smaller systems that the ground state at these filling factors is indeed fully spin-polarized [46]. As shown in the Supplemental Material, we also find evidence for an anomalous composite Fermi liquid at $n = \frac{1}{2}$ [46, 78, 79].

Discussion — We have therefore demonstrated a mechanism by which topological flat bands and fractionalized phases can be realized in narrow gap semiconductor films using only an electrostatic superlattice potential. Due to the generality of our mechanism, and high degree of flexibility in terms of material choice, film thickness, and superlattice potential, our theory provides a potential pathway to realizing fractionalized topological phases in new platforms and potentially higher temperatures. In moiré materials, the chemistry at the van der Waals interface plays a key role: properties such as the interlayer tunneling are difficult to tune (requiring, for instance, high pressure [76, 80–82]). As a result, models are typically material-specific and it is not clear how to extend the observed fractionalized states to higher temperatures. In contrast, our proposed mechanism is not tied to a specific material realization, allowing for a great degree of

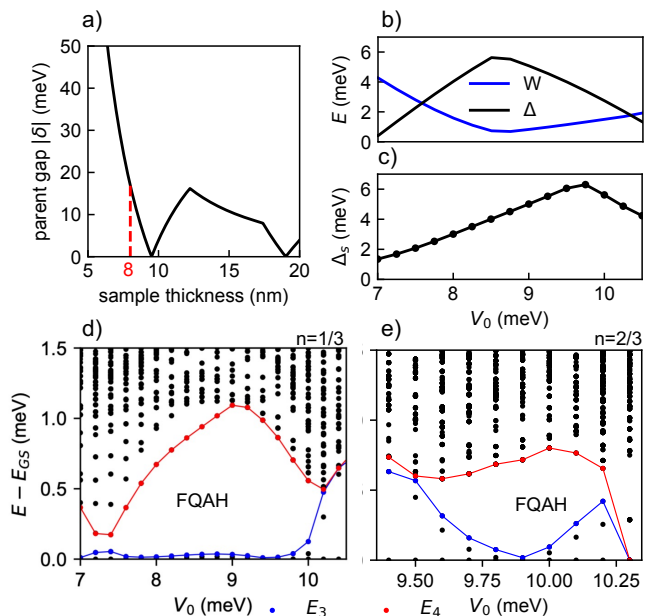


FIG. 4. Results for Cd_3As_2 thin film. (a) Parent bandgap $|\delta|$ as a function of its thickness, $L = 8$ nm is chosen based on the criterion discussed in the main text. (b) Lowest valence mini-bandwidth W and minimum direct gap Δ as a function of superlattice potential strength V_0 . (c) Magnon gap $\Delta_s = E(S_z^{\text{max}} - 1) - E(S_z^{\text{max}})$ at $n = 1$ as a function of V_0 , demonstrating a robust $|C| = 1$ QAH state. Evolution of low-energy spectrum within the maximum S_z sector at (d) $n = \frac{1}{3}$ and (e) $\frac{2}{3}$ as a function of V_0 , showing FQAH states. The effective parameters are: $\delta = 16.9$ meV, $v = 88.9$ meVnm, $\alpha_1 = 250$ nm², $\alpha_2 = 20$ meVnm² [46]; $a = 20$ nm, $\phi = 0$, and $\epsilon = 10$. The finite system used contains 27 superlattice unit cells.

freedom in device design and optimization.

The critical temperature of fractionalized states is mostly set by the Coulomb interaction scale $E_C \sim \frac{e^2}{\epsilon a}$. While we have focused on $a = 20$ nm superlattice period for Cd_3As_2 , this is not a fine-tuned choice since flat bands can be realized for a broad range of g (see Fig 2(a,b)), and we find similar physics at smaller periods as well [46]. Thus, depending on the material properties and experimentally accessible superlattice potential strengths and periods, higher temperature fractionalized states can, in principle, be engineered through this mechanism.

The idea of using of superlattice potential for realizing FCIs has been explored in the context of multilayer graphene [39, 40]. The main distinction of our work is that we go beyond simply showing the existence of FCIs: we provide a robust physical picture for why a topological flat band with optimized quantum geometry must emerge in this model. This approach allows us to generalize our findings beyond any one specific material.

The essential ingredient for the active layer in our theory is a 2D narrow gap semiconductor described at low energy by the universal Hamiltonian, Eq 1. Potential candidates include thin films of: 3D topological insula-

tors [83] (e.g. Bi_2Te_3 , Bi_2Se_3 , Sb_2Te_3 , Sb_2Se_3), IV-VI semiconductors (SnTe , PbTe) [84, 85], 3D Dirac semimetals (Cd_3As_2) [69, 72], or Bi [44, 86, 87]. In this work, we have used our theory to identify and predict fractionalized states in Cd_3As_2 . We expect that such physics is possible in many other materials as well (similar results for Sb_2Te_3 are shown in the supplemental material [46]). A full systematic analysis of candidate materials is an important subject for future study.

There are many potential avenues to realize the control layer. One possibility is a doped moiré superlattice, such as a TMD heterobilayer [88], in which the doped electrons or holes are localized at the most energetically favorable stacking configurations, typically forming a triangular lattice. The system exhibits a modulated charge density, leading to a periodic electrostatic potential felt by the nearby active layer [22–24]. The period can be tuned by choosing materials with different atomic mismatch or applying a twist; and the potential strength can be adjusted by tuning the density of doped electrons or holes. Another possibility for realizing a superlattice potential is via the twist interface of hBN or TMD [26–30, 36]. Another interesting approach is that the periodic potential may be generated spontaneously via a charge-ordering induced at the interface [89–92]. An effective potential can also be generated via a moiré at

the interface with a monolayer material [93]. Other ways to engineer superlattice potentials include patterned dielectrics [25, 31–35], or $\text{LaAlO}_3/\text{SrTiO}_3$ interface patterned by conductive atomic force microscope lithography [94].

In conclusion, we have presented a route by which topological and fractionalized phases may be realized in a large class of narrow gap semiconductor films. Our results opens up new possibilities for engineered quantum materials that may offer even greater flexibility and richness than existing moiré materials.

ACKNOWLEDGMENTS

We thank Aviram Uri, Aaron Sharpe, Ahmed Abouelkomsan, Jia Li, and Long Ju for helpful comments on the manuscript and for valuable discussions. TD acknowledges support from a startup fund at Stanford University. TT is supported by the Stanford Graduate fellowship. The work at Massachusetts Institute of Technology was supported by the Air Force Office of Scientific Research (AFOSR) under Award No. FA9550-22-1-0432. The authors acknowledge the MIT SuperCloud and Lincoln Laboratory Supercomputing Center for providing HPC resources that have contributed to the research results reported within this paper.

-
- [1] D. Sheng, Z.-C. Gu, K. Sun, and L. Sheng, Fractional quantum hall effect in the absence of Landau levels, *Nature communications* **2**, 389 (2011).
 - [2] T. Neupert, L. Santos, C. Chamon, and C. Mudry, Fractional quantum hall states at zero magnetic field, *Physical review letters* **106**, 236804 (2011).
 - [3] N. Regnault and B. A. Bernevig, Fractional Chern insulator, *Physical Review X* **1**, 021014 (2011).
 - [4] K. Sun, Z. Gu, H. Katsura, and S. D. Sarma, Nearly flatbands with nontrivial topology, *Physical review letters* **106**, 236803 (2011).
 - [5] E. Tang, J.-W. Mei, and X.-G. Wen, High-temperature fractional quantum hall states, *Physical review letters* **106**, 236802 (2011).
 - [6] S. A. Parameswaran, R. Roy, and S. L. Sondhi, Fractional quantum hall physics in topological flat bands, *Comptes Rendus Physique* **14**, 816 (2013).
 - [7] Z. Liu and E. J. Bergholtz, Recent developments in fractional Chern insulators, *arXiv preprint arXiv:2208.08449* (2022).
 - [8] E. Y. Andrei, D. K. Efetov, P. Jarillo-Herrero, A. H. MacDonald, K. F. Mak, T. Senthil, E. Tutuc, A. Yazdani, and A. F. Young, The marvels of moiré materials, *Nature Reviews Materials* **6**, 201 (2021).
 - [9] K. F. Mak and J. Shan, Semiconductor moiré materials, *Nature Nanotechnology* **17**, 686 (2022).
 - [10] R. Bistritzer and A. H. MacDonald, Moiré bands in twisted double-layer graphene, *Proceedings of the National Academy of Sciences* **108**, 12233 (2011).
 - [11] E. S. Morell, J. Correa, P. Vargas, M. Pacheco, and Z. Barticevic, Flat bands in slightly twisted bilayer graphene: Tight-binding calculations, *Physical Review B* **82**, 121407 (2010).
 - [12] F. Wu, T. Lovorn, E. Tutuc, I. Martin, and A. MacDonald, Topological insulators in twisted transition metal dichalcogenide homobilayers, *Physical review letters* **122**, 086402 (2019).
 - [13] H. Li, U. Kumar, K. Sun, and S.-Z. Lin, Spontaneous fractional Chern insulators in transition metal dichalcogenide moiré superlattices, *Physical Review Research* **3**, L032070 (2021).
 - [14] V. Crépel and L. Fu, Anomalous hall metal and fractional Chern insulator in twisted transition metal dichalcogenides, *Physical Review B* **107**, L201109 (2023).
 - [15] J. Cai, E. Anderson, C. Wang, X. Zhang, X. Liu, W. Holtzmann, Y. Zhang, F. Fan, T. Taniguchi, K. Watanabe, *et al.*, Signatures of fractional quantum anomalous hall states in twisted mote_2 , *Nature* **622**, 63 (2023).
 - [16] Y. Zeng, Z. Xia, K. Kang, J. Zhu, P. Knüppel, C. Vaswani, K. Watanabe, T. Taniguchi, K. F. Mak, and J. Shan, Thermodynamic evidence of fractional Chern insulator in moiré mote_2 , *Nature*, 1 (2023).
 - [17] H. Park, J. Cai, E. Anderson, Y. Zhang, J. Zhu, X. Liu, C. Wang, W. Holtzmann, C. Hu, Z. Liu, *et al.*, Observation of fractionally quantized anomalous hall effect, *Nature* **622**, 74 (2023).

- [18] F. Xu, Z. Sun, T. Jia, C. Liu, C. Xu, C. Li, Y. Gu, K. Watanabe, T. Taniguchi, B. Tong, *et al.*, Observation of integer and fractional quantum anomalous hall states in twisted bilayer mote2, arXiv preprint arXiv:2308.06177 (2023).
- [19] Z. Lu, T. Han, Y. Yao, A. P. Reddy, J. Yang, J. Seo, K. Watanabe, T. Taniguchi, L. Fu, and L. Ju, Fractional quantum anomalous hall effect in a graphene moire superlattice, arXiv preprint arXiv:2309.17436 (2023).
- [20] C. N. Lau, M. W. Bockrath, K. F. Mak, and F. Zhang, Reproducibility in the fabrication and physics of moiré materials, *Nature* **602**, 41 (2022).
- [21] H. L. Stormer, D. C. Tsui, and A. C. Gossard, The fractional quantum hall effect, *Reviews of Modern Physics* **71**, S298 (1999).
- [22] J. Gu, K. Watanabe, T. Taniguchi, J. Shan, and K. F. Mak, Remote imprinting of moiré lattices, *Research Square* (2023).
- [23] Z. Zhang, J. Xie, W. Zhao, R. Qi, C. Sanborn, S. Wang, S. Kahn, K. Watanabe, T. Taniguchi, A. Zettl, *et al.*, Engineering correlated insulators in bilayer graphene with a remote coulomb superlattice, *Nature Materials*, 1 (2024).
- [24] M. He, J. Cai, H. Zheng, E. Seewald, T. Taniguchi, K. Watanabe, J. Yan, M. Yankowitz, A. Pasupathy, W. Yao, *et al.*, Dynamically tunable moiré exciton rydberg states in a monolayer semiconductor on twisted bilayer graphene, *Nature Materials*, 1 (2024).
- [25] C. Forsythe, X. Zhou, K. Watanabe, T. Taniguchi, A. Pasupathy, P. Moon, M. Koshino, P. Kim, and C. R. Dean, Band structure engineering of 2d materials using patterned dielectric superlattices, *Nature nanotechnology* **13**, 566 (2018).
- [26] K. Yasuda, X. Wang, K. Watanabe, T. Taniguchi, and P. Jarillo-Herrero, Stacking-engineered ferroelectricity in bilayer boron nitride, *Science* **372**, 1458 (2021).
- [27] X. Wang, K. Yasuda, Y. Zhang, S. Liu, K. Watanabe, T. Taniguchi, J. Hone, L. Fu, and P. Jarillo-Herrero, Interfacial ferroelectricity in rhombohedral-stacked bilayer transition metal dichalcogenides, *Nature nanotechnology* **17**, 367 (2022).
- [28] P. Zhao, C. Xiao, and W. Yao, Universal superlattice potential for 2d materials from twisted interface inside h-bn substrate, *npj 2D Materials and Applications* **5**, 38 (2021).
- [29] D. S. Kim, R. C. Dominguez, R. Mayorga-Luna, D. Ye, J. Embley, T. Tan, Y. Ni, Z. Liu, M. Ford, F. Y. Gao, *et al.*, Electrostatic moiré potential from twisted hexagonal boron nitride layers, *Nature materials*, 1 (2023).
- [30] C. Woods, P. Ares, H. Nevison-Andrews, M. Holwill, R. Fabregas, F. Guinea, A. Geim, K. Novoselov, N. Walet, and L. Fumagalli, Charge-polarized interfacial superlattices in marginally twisted hexagonal boron nitride, *Nature communications* **12**, 347 (2021).
- [31] L.-k. Shi, J. Ma, and J. C. Song, Gate-tunable flat bands in van der waals patterned dielectric superlattices, *2D Materials* **7**, 015028 (2019).
- [32] Y. Xu, C. Horn, J. Zhu, Y. Tang, L. Ma, L. Li, S. Liu, K. Watanabe, T. Taniguchi, J. C. Hone, *et al.*, Creation of moiré bands in a monolayer semiconductor by spatially periodic dielectric screening, *Nature Materials* **20**, 645 (2021).
- [33] D. Barcons Ruiz, H. Herzig Sheinflux, R. Hoffmann, I. Torre, H. Agarwal, R. K. Kumar, L. Vistoli, T. Taniguchi, K. Watanabe, A. Bachtold, *et al.*, Engineering high quality graphene superlattices via ion milled ultra-thin etching masks, *Nature Communications* **13**, 6926 (2022).
- [34] J. Sun, S. A. A. Ghorashi, K. Watanabe, T. Taniguchi, F. Camino, J. Cano, and X. Du, Signature of correlated insulator in electric field controlled superlattice, arXiv preprint arXiv:2306.06848 (2023).
- [35] Y. Li, S. Dietrich, C. Forsythe, T. Taniguchi, K. Watanabe, P. Moon, and C. R. Dean, Anisotropic band flattening in graphene with one-dimensional superlattices, *Nature Nanotechnology* **16**, 525 (2021).
- [36] X. Wang, C. Xu, S. Aronson, D. Bennett, N. Paul, P. J. D. Crowley, C. Collignon, K. Watanabe, T. Taniguchi, R. Ashoori, E. Kaxiras, Y. Zhang, P. Jarillo-Herrero, and K. Yasuda, Band structure engineering using a moiré polar substrate (2024), arXiv:2405.03761 [cond-mat.mes-hall].
- [37] J. C. Song, P. Samutpraphoot, and L. S. Levitov, Topological bloch bands in graphene superlattices, *Proceedings of the National Academy of Sciences* **112**, 10879 (2015).
- [38] R. Huber, M.-H. Liu, S.-C. Chen, M. Drienovsky, A. Sandner, K. Watanabe, T. Taniguchi, K. Richter, D. Weiss, and J. Eroms, Gate-tunable two-dimensional superlattices in graphene, *Nano letters* **20**, 8046 (2020).
- [39] S. A. A. Ghorashi, A. Dunbrack, A. Abouelkomsan, J. Sun, X. Du, and J. Cano, Topological and stacked flat bands in bilayer graphene with a superlattice potential, *Physical Review Letters* **130**, 196201 (2023).
- [40] S. A. A. Ghorashi and J. Cano, Multilayer graphene with a superlattice potential, *Physical Review B* **107**, 195423 (2023).
- [41] Y. Zeng, T. M. R. Wolf, C. Huang, N. Wei, S. A. A. Ghorashi, A. H. MacDonald, and J. Cano, Gate-tunable topological phases in superlattice modulated bilayer graphene (2024), arXiv:2401.04321 [cond-mat.mes-hall].
- [42] C. Albrecht, J. Smet, D. Weiss, K. Von Klitzing, R. Henning, M. Langenbuch, M. Suhrke, U. Rössler, V. Umansky, and H. Schweizer, Fermiology of two-dimensional lateral superlattices, *Physical review letters* **83**, 2234 (1999).
- [43] D. Q. Wang, Z. Krix, O. A. Tkachenko, V. A. Tkachenko, C. Chen, I. Farrer, D. A. Ritchie, O. P. Sushkov, A. R. Hamilton, and O. Klochan, Tuning the bandstructure of electrons in a two-dimensional artificial electrostatic crystal in gaas quantum wells, arXiv preprint arXiv:2402.12769 (2024).
- [44] L. Fu and C. L. Kane, Topological insulators with inversion symmetry, *Physical Review B* **76**, 045302 (2007).
- [45] B. A. Bernevig, T. L. Hughes, and S.-C. Zhang, Quantum spin hall effect and topological phase transition in hgte quantum wells, *science* **314**, 1757 (2006).
- [46] See the supplementary information for (1) more detailed properties of the bands near the magic point, (2) symmetry analysis of k.p model, (3) additional details on the many-body calculation, (4) detailed discussion on the massive Dirac fermion model, (5) detailed discussion of modeling real materials, which includes Refs.[95–106].
- [47] Y. Su, H. Li, C. Zhang, K. Sun, and S.-Z. Lin, Massive dirac fermions in moiré superlattices: A route towards topological flat minibands and correlated topological insulators, *Physical Review Research* **4**, 10.1103/physrevresearch.4.1032024 (2022).

- [48] N. Suri, C. Wang, B. M. Hunt, and D. Xiao, Superlattice engineering of topology in massive dirac fermions, arXiv preprint arXiv:2305.13522 (2023).
- [49] S. Parameswaran, R. Roy, and S. L. Sondhi, Fractional chern insulators and the ∞ algebra, *Physical Review B* **85**, 241308 (2012).
- [50] R. Roy, Band geometry of fractional topological insulators, *Physical Review B* **90**, 165139 (2014).
- [51] M. Claassen, C. H. Lee, R. Thomale, X.-L. Qi, and T. P. Devereaux, Position-momentum duality and fractional quantum hall effect in chern insulators, *Physical review letters* **114**, 236802 (2015).
- [52] T. S. Jackson, G. Möller, and R. Roy, Geometric stability of topological lattice phases, *Nature communications* **6**, 8629 (2015).
- [53] J. Wang, J. Cano, A. J. Millis, Z. Liu, and B. Yang, Exact landau level description of geometry and interaction in a flatband, *Physical review letters* **127**, 246403 (2021).
- [54] P. J. Ledwith, G. Tarnopolsky, E. Khalaf, and A. Vishwanath, Fractional chern insulator states in twisted bilayer graphene: An analytical approach, *Physical Review Research* **2**, 023237 (2020).
- [55] P. J. Ledwith, A. Vishwanath, and D. E. Parker, Vortexability: A unifying criterion for ideal fractional chern insulators, arXiv preprint arXiv:2209.15023 (2022).
- [56] E. Khalaf, A. J. Kruchkov, G. Tarnopolsky, and A. Vishwanath, Magic angle hierarchy in twisted graphene multilayers, *Physical Review B* **100**, 085109 (2019).
- [57] T. Devakul, V. Crépel, Y. Zhang, and L. Fu, Magic in twisted transition metal dichalcogenide bilayers, *Nature communications* **12**, 6730 (2021).
- [58] T. Devakul, P. J. Ledwith, L.-Q. Xia, A. Uri, S. C. de la Barrera, P. Jarillo-Herrero, and L. Fu, Magic-angle helical trilayer graphene, *Science Advances* **9**, eadi6063 (2023).
- [59] N. Morales-Durán, N. Wei, and A. H. MacDonald, Magic angles and fractional chern insulators in twisted homobilayer tmds, arXiv preprint arXiv:2308.03143 (2023).
- [60] A. P. Reddy and L. Fu, Toward a global phase diagram of the fractional quantum anomalous hall effect, *Phys. Rev. B* **108**, 245159 (2023).
- [61] V. Crépel, N. Regnault, and R. Queiroz, The chiral limits of moiré semiconductors: origin of flat bands and topology in twisted transition metal dichalcogenides homobilayers, arXiv preprint arXiv:2305.10477 (2023).
- [62] A. P. Reddy, F. Alsallom, Y. Zhang, T. Devakul, and L. Fu, Fractional quantum anomalous hall states in twisted bilayer MoTe_2 and WSe_2 , *Phys. Rev. B* **108**, 085117 (2023).
- [63] Y. Fu, E. J. König, J. H. Wilson, Y.-Z. Chou, and J. H. Pixley, Magic-angle semimetals, *npj Quantum Materials* **5**, 71 (2020).
- [64] Y. Fu, J. H. Wilson, and J. Pixley, Flat topological bands and eigenstate criticality in a quasiperiodic insulator, *Physical Review B* **104**, L041106 (2021).
- [65] Z. Wang, H. Weng, Q. Wu, X. Dai, and Z. Fang, Three-dimensional dirac semimetal and quantum transport in Cd_3As_2 , *Physical Review B* **88**, 125427 (2013).
- [66] N. Armitage, E. Mele, and A. Vishwanath, Weyl and dirac semimetals in three-dimensional solids, *Reviews of Modern Physics* **90**, 015001 (2018).
- [67] S. Borisenko, Q. Gibson, D. Evtushinsky, V. Zabolotnyy, B. Büchner, and R. J. Cava, Experimental realization of a three-dimensional dirac semimetal, *Physical review letters* **113**, 027603 (2014).
- [68] M. Neupane, S.-Y. Xu, R. Sankar, N. Alidoust, G. Bian, C. Liu, I. Belopolski, T.-R. Chang, H.-T. Jeng, H. Lin, *et al.*, Observation of a three-dimensional topological dirac semimetal phase in high-mobility Cd_3As_2 , *Nature communications* **5**, 3786 (2014).
- [69] Z. Liu, J. Jiang, B. Zhou, Z. Wang, Y. Zhang, H. Weng, D. Prabhakaran, S. K. Mo, H. Peng, P. Dudin, *et al.*, A stable three-dimensional topological dirac semimetal Cd_3As_2 , *Nature materials* **13**, 677 (2014).
- [70] M. N. Ali, Q. Gibson, S. Jeon, B. B. Zhou, A. Yazdani, and R. J. Cava, The crystal and electronic structures of Cd_3As_2 , the three-dimensional electronic analogue of graphene, *Inorganic chemistry* **53**, 4062 (2014).
- [71] I. Crassee, R. Sankar, W.-L. Lee, A. Akrap, and M. Orlita, 3d dirac semimetal Cd_3As_2 : A review of material properties, *Physical Review Materials* **2**, 120302 (2018).
- [72] A. C. Lygo, B. Guo, A. Rashidi, V. Huang, P. Cuadros-Romero, and S. Stemmer, Two-dimensional topological insulator state in cadmium arsenide thin films, *Physical Review Letters* **130**, 046201 (2023).
- [73] J. Cano, B. Bradlyn, Z. Wang, M. Hirschberger, N. P. Ong, and B. A. Bernevig, Chiral anomaly factory: Creating weyl fermions with a magnetic field, *Physical Review B* **95**, 161306 (2017).
- [74] S. Baidya and D. Vanderbilt, First-principles theory of the dirac semimetal Cd_3As_2 under zeeman magnetic field, *Physical Review B* **102**, 165115 (2020).
- [75] W. Miao, B. Guo, S. Stemmer, and X. Dai, Engineering the in-plane anomalous hall effect in Cd_3As_2 thin films, arXiv preprint arXiv:2309.15457 (2023).
- [76] N. Morales-Durán, J. Wang, G. R. Schleder, M. Angeli, Z. Zhu, E. Kaxiras, C. Repellin, and J. Cano, Pressure-enhanced fractional chern insulators along a magic line in moiré transition metal dichalcogenides, *Physical Review Research* **5**, L032022 (2023).
- [77] P. Wilhelm, T. C. Lang, and A. M. Läuchli, Interplay of fractional chern insulator and charge density wave phases in twisted bilayer graphene, *Physical Review B* **103**, 125406 (2021).
- [78] H. Goldman, A. P. Reddy, N. Paul, and L. Fu, Zero-field composite fermi liquid in twisted semiconductor bilayers, arXiv preprint arXiv:2306.02513 (PRL in press) (2023).
- [79] J. Dong, J. Wang, P. J. Ledwith, A. Vishwanath, and D. E. Parker, Composite fermi liquid at zero magnetic field in twisted MoTe_2 , arXiv preprint arXiv:2306.01719 (2023).
- [80] M. Yankowitz, J. Jung, E. Laksono, N. Leconte, B. L. Chittari, K. Watanabe, T. Taniguchi, S. Adam, D. Graf, and C. R. Dean, Dynamic band-structure tuning of graphene moiré superlattices with pressure, *Nature* **557**, 404 (2018).
- [81] M. Yankowitz, S. Chen, H. Polshyn, Y. Zhang, K. Watanabe, T. Taniguchi, D. Graf, A. F. Young, and C. R. Dean, Tuning superconductivity in twisted bilayer graphene, *Science* **363**, 1059 (2019).
- [82] S. Carr, S. Fang, P. Jarillo-Herrero, and E. Kaxiras, Pressure dependence of the magic twist angle in graphene superlattices, *Physical Review B* **98**, 085144 (2018).

- [83] M. Z. Hasan and C. L. Kane, Colloquium: topological insulators, *Reviews of modern physics* **82**, 3045 (2010).
- [84] T. H. Hsieh, H. Lin, J. Liu, W. Duan, A. Bansil, and L. Fu, Topological crystalline insulators in the sntc material class, *Nature communications* **3**, 982 (2012).
- [85] J. Liu and L. Fu, Electrically tunable quantum spin hall state in topological crystalline insulator thin films, *Physical Review B* **91**, 081407 (2015).
- [86] S. Murakami, Quantum spin hall effect and enhanced magnetic response by spin-orbit coupling, *Physical Review Letters* **97**, 236805 (2006).
- [87] L. Chen, A. X. Wu, N. Tulu, J. Wang, A. Juanson, K. Watanabe, T. Taniguchi, M. T. Pettes, M. Campbell, C. A. Gadre, Y. Zhou, H. Chen, P. Cao, L. A. Jauregui, R. Wu, X. Pan, and J. D. Sanchez-Yamagishi, Exceptional electronic transport and quantum oscillations in thin bismuth crystals grown inside van der waals materials (2023), arXiv:2211.07681 [cond-mat.mes-hall].
- [88] F. Wu, T. Lovorn, and E. Tutuc, Hubbard model physics in transition metal dichalcogenide moiré bands, *Physical review letters* **121**, 026402 (2018).
- [89] X. Lu, S. Zhang, Y. Wang, X. Gao, K. Yang, Z. Guo, Y. Gao, Y. Ye, Z. Han, and J. Liu, Synergistic correlated states and nontrivial topology in coupled graphene-insulator heterostructures, *Nature Communications* **14**, 5550 (2023).
- [90] C.-C. Tseng, T. Song, Q. Jiang, Z. Lin, C. Wang, J. Suh, K. Watanabe, T. Taniguchi, M. A. McGuire, D. Xiao, *et al.*, Gate-tunable proximity effects in graphene on layered magnetic insulators, *Nano Letters* **22**, 8495 (2022).
- [91] K. Yang, X. Gao, Y. Wang, T. Zhang, Y. Gao, X. Lu, S. Zhang, J. Liu, P. Gu, Z. Luo, *et al.*, Unconventional correlated insulator in crocl-interfaced bernal bilayer graphene, *Nature Communications* **14**, 2136 (2023).
- [92] Y. Wang, X. Gao, K. Yang, P. Gu, X. Lu, S. Zhang, Y. Gao, N. Ren, B. Dong, Y. Jiang, *et al.*, Quantum hall phase in graphene engineered by interfacial charge coupling, *Nature Nanotechnology* **17**, 1272 (2022).
- [93] K. Yang, Z. Xu, Y. Feng, F. Schindler, Y. Xu, Z. Bi, B. A. Bernevig, P. Tang, and C.-X. Liu, Z_2 -nontrivial moire minibands and interaction-driven quantum anomalous hall insulators in topological insulator based moire heterostructures, arXiv preprint arXiv:2304.09907 (2023).
- [94] Y.-Y. Pai, A. Tylan-Tyler, P. Irvin, and J. Levy, Physics of struo3-based heterostructures and nanostructures: a review, *Reports on Progress in Physics* **81**, 036503 (2018).
- [95] E. Rezayi and N. Read, Fermi-liquid-like state in a half-filled landau level, *Physical review letters* **72**, 900 (1994).
- [96] S. D. Geraedts, J. Wang, E. Rezayi, and F. Haldane, Berry phase and model wave function in the half-filled landau level, *Physical review letters* **121**, 147202 (2018).
- [97] M. Fremling, N. Moran, J. Slingerland, and S. H. Simon, Trial wave functions for a composite fermi liquid on a torus, *Physical Review B* **97**, 035149 (2018).
- [98] J. Wang, S. D. Geraedts, E. Rezayi, and F. Haldane, Lattice monte carlo for quantum hall states on a torus, *Physical Review B* **99**, 125123 (2019).
- [99] J. Wang, Dirac fermion hierarchy of composite fermi liquids, *Physical review letters* **122**, 257203 (2019).
- [100] A. Stern and L. Fu, Transport properties of a half-filled chern band at the electron and composite fermion phases, arXiv preprint arXiv:2311.16761 (2023).
- [101] C. Fang, M. J. Gilbert, and B. A. Bernevig, Bulk topological invariants in noninteracting point group symmetric insulators, *Physical Review B* **86**, 115112 (2012).
- [102] T. Wang, N. F. Yuan, and L. Fu, Moiré surface states and enhanced superconductivity in topological insulators, *Physical Review X* **11**, 021024 (2021).
- [103] J. Cano, S. Fang, J. Pixley, and J. H. Wilson, Moiré superlattice on the surface of a topological insulator, *Physical Review B* **103**, 155157 (2021).
- [104] H.-Z. Lu, W.-Y. Shan, W. Yao, Q. Niu, and S.-Q. Shen, Massive dirac fermions and spin physics in an ultrathin film of topological insulator, *Physical review B* **81**, 115407 (2010).
- [105] C.-X. Liu, X.-L. Qi, H. Zhang, X. Dai, Z. Fang, and S.-C. Zhang, Model hamiltonian for topological insulators, *Physical Review B* **82**, 045122 (2010).
- [106] J. Cano, B. Bradlyn, Z. Wang, M. Hirschberger, N. P. Ong, and B. A. Bernevig, Chiral anomaly factory: Creating weyl fermions with a magnetic field, *Physical Review B* **95**, 10.1103/physrevb.95.161306 (2017).
- [107] Assume it is $(c_1 k_x + c_2 k_y)\sigma_z s_x + (c_3 k_x + c_4 k_y)\sigma_z s_y$, then rotational symmetry requires $c_1 = c_4$, and $c_2 = c_3 = 0$.

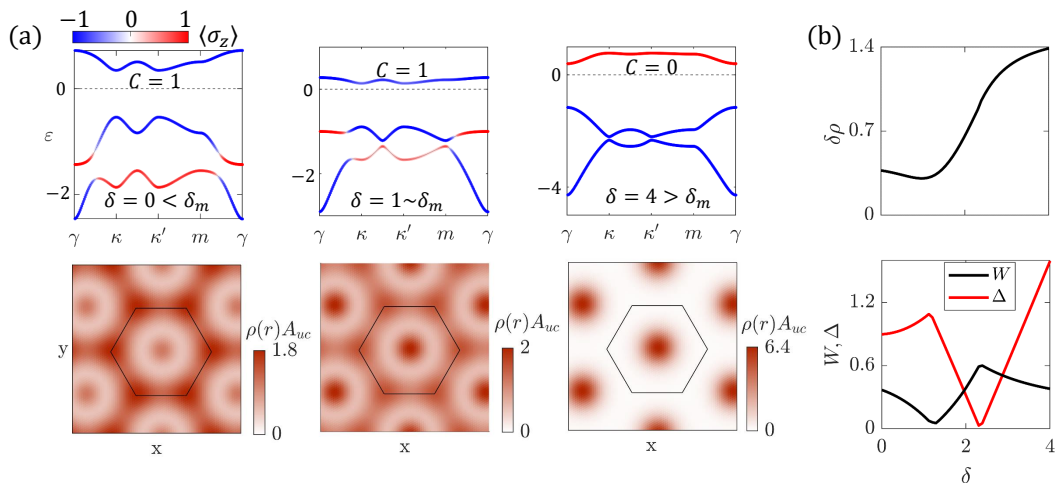


FIG. S1. Evolution of the real-space charge density. **(a)** Band structure (top) and real space charge density of the first conduction miniband (bottom) as δ is tuned. The color of the bands indicates the $\langle \sigma_z \rangle$ expectation value. The Chern numbers of the first conduction miniband is labeled. We showed three scenarios: $\delta = 0 < \delta_m$ (deep-inverted), $\delta = 1.0 \sim \delta_m$ (the magic value), $\delta = 4.0 > \delta_m$ (before inversion). **(b)** The top panel is the $\delta\rho$ as δ is tuned through the magic value. The bottom panel is the corresponding direct gap Δ and bandwidth W . The parameter used is $V_0 = 1$ and $g = 2$, $\phi = \pi$ (The same as the main text figures. So the bottom panel is a section of the main text figures.).

Appendix A: More on magic near parent band inversion

We measure all the quantities in units of E_D and k_D and suppress these two symbols in this section.

1. Real space charge density migration

As we argued in the main text, at large δ with $\phi = 60^\circ$, the wave function of first conduction miniband will be localized on the triangular minimum of the potential. At deep inversion $\delta < \delta_m$, the first conduction miniband will be localized on the honeycomb maximum of the potential. The interpolation between these two extreme scenario shows a magic point where the real space charge density is most uniform. We define a metric for this non-uniformity

$$(\delta\rho)^2 = A_{uc} \int_{unitcell} d\mathbf{r} (\rho(\mathbf{r}) - \bar{\rho})^2 \quad (\text{A1})$$

As plotted in Fig.S1, indeed we observe such interpolation and the corresponding minimum of $\delta\rho$ occur at approximately at δ_m .

2. Quantum geometry at $g = 2$ and $g = 3$

We mentioned that the mechanism for generating magic bands is naturally associated with the spreading out of the berry curvature. We showed only the bandwidth and the gap in the main text. Here, we further show two quantum geometric indicators, the Berry curvature (BC) non-uniformity δf and trace condition violation \bar{T} , defined

$$(\delta f)^2 = \frac{A_{mBZ}}{4\pi^2} \int (f(k) - \bar{f})^2 d\mathbf{k} \quad (\text{A2})$$

$$\bar{T} = \int (\text{Tr}[g_{\mu\nu}^{FS}(k)] - |f(k)|) d\mathbf{k} \quad (\text{A3})$$

They are shown as a function of δ and V_0 for $g = 2$ in Fig S2, and for $g = 3$ in Fig S3. Both δf and \bar{T} are very small near the magic line at which bandwidth is minimized, indicating favorable conditions for fractional states. Fig S3 also serves to demonstrate that the precise choice of $g = 2$ to show in the main text is not a fine-tuned choice.

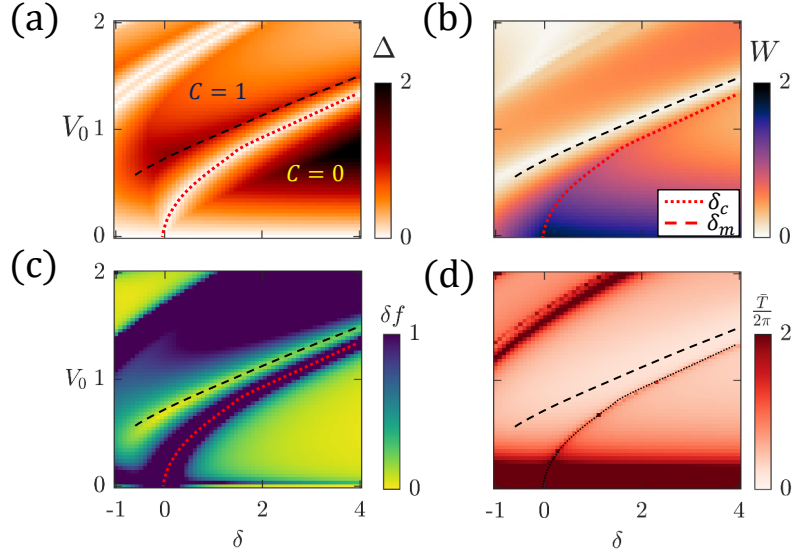


FIG. S2. Energetic and geometric properties of the flat band at $g = 2$. The (a) direct gap Δ , (b) bandwidth W , (c) Berry curvature standard deviation δf , and (d) trace-condition violation \bar{T} of the first conduction miniband as a function of potential strength V_0 and inversion depth δ of the band inversion model introduced in the main text in a triangular lattice potential with $g = 2$, $\phi = \pi$. The miniband inversion δ_c and the magic δ_m are shown as dotted and dashed lines.

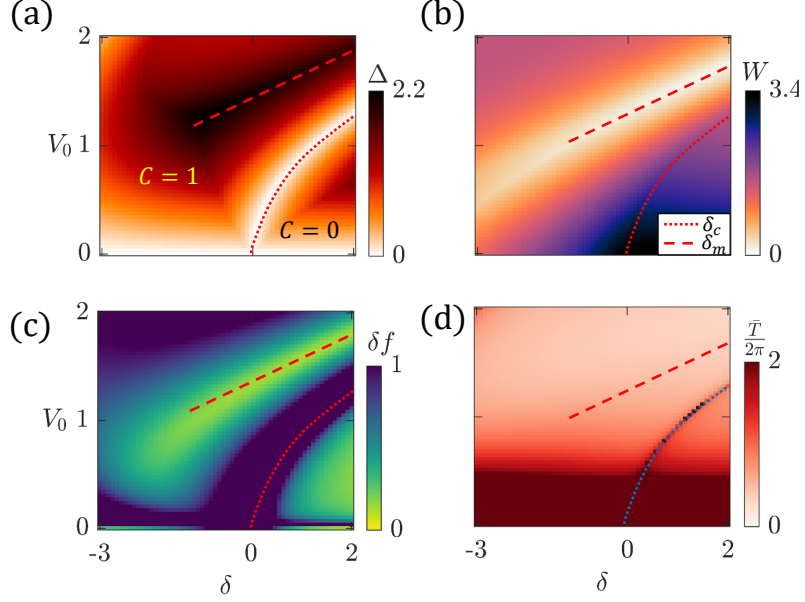


FIG. S3. Same as Fig S2 but with $g = 3$.

3. Magic at $\phi = \pi/6$

In the main text, we have discussed the case with a perfect triangular potential $\phi = \pi$ (and also honeycomb by particle-hole transformation.). Here, we consider a $\phi = \pi/6$ potential, which is easily achievable with a control layer made of twisted hBN [28, 29]. This potential has one potential maximum and one minimum per unit cell, which forms two offset triangular lattices. The origin of this potential arises from the spatially periodic out-of-plane electric polarization in twisted hBN which points downward at the AB regions, and upward at the BA regions. This electric polarization leads to an electrostatic potential felt by a nearby layer with both attractive and repulsive potential sites.

With this kind of potential, at large δ , i.e. uninverted, the first conduction/valence will have their minimum/maximum point at γ . Both bands will have $C = 0$ as a result of their C_3 eigenvalue at the high symmetry points of mBZ. Notice also that these two bands only have the same C_3 eigenvalue at one of the valleys (say κ).

As we slowly decrease δ , these two bands will first invert at γ (first column of Fig. S4 (a)), resulting in the miniband having a concentrated BC at γ . As we further decrease δ , the two bands also get inverted at κ and κ' . At κ' , due to the difference in C_3 eigenvalue, the first conduction band will then have a concentrated BC around κ' (third column of Fig. S4 (a)). The interpolation between these two gives us the optimal point where the various band quantum geometry quantities are optimized (second column of Fig. S4 (a)).

These quantities are summarized in Fig S4(b). While there is still an optimal point, we find that the bandwidth-to-bandgap ratio, δf , and \bar{T} are not as ideal as for the perfect triangular lattice potential.

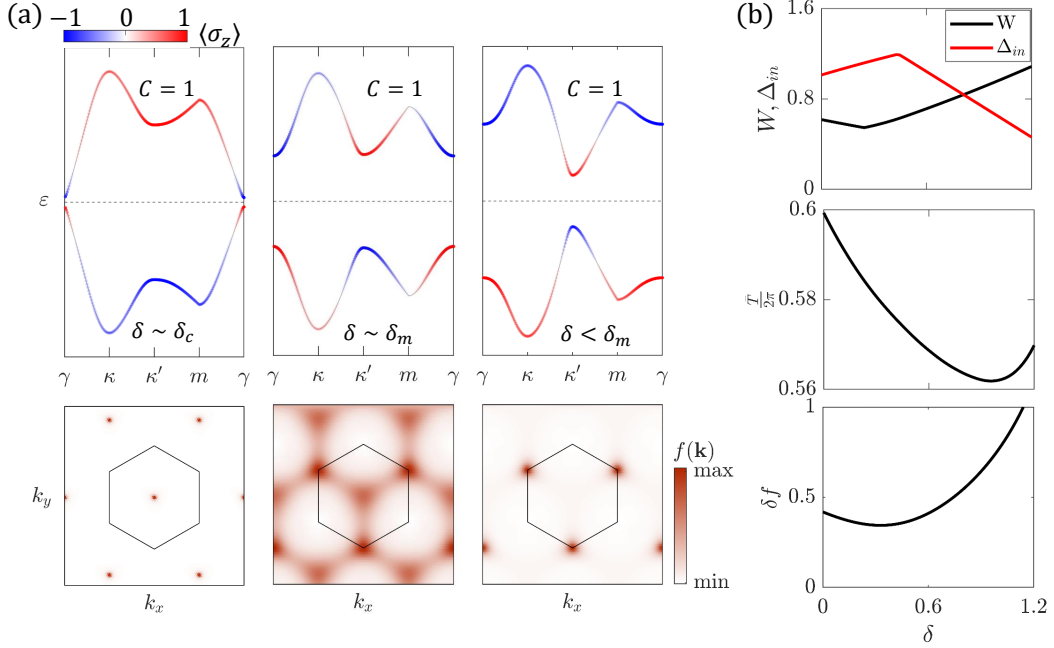


FIG. S4. Tuning to the flat band with a $\phi = \pi/6$ potential. **(a)** Schematic figure illustrating the miniband inversion as δ is tuned. The color indicates the $\langle \sigma_z \rangle$ expectation value. The Chern numbers of the first conduction miniband is labeled. We showed three scenarios: $\delta \sim \delta_c$ (right after inversion), $\delta = \delta_m$ (the magic value), $\delta < \delta_m$ (below the magic value). The bottom panel is the corresponding BC distribution. **(b)** Bandwidth W , indirect gap Δ_{in} , trace condition violation \bar{T} , BC non-uniformity δf as a function of δ . The parameter used is $V_0 = 1$, $g = 2.5$, $\phi = \frac{\pi}{6}$.

Appendix B: Symmetry Analysis

We claim in the main text that the starting point of our Hamiltonian is the most general one consistent with all the symmetry constraint. We prove the claim in this section. We denote the Pauli matrices in the spin subspace by s and the Pauli matrices in the orbital subspace by σ .

The symmetry constraint of the system is parity symmetry P , time reversal symmetry $T^2 = -1$, and rotational symmetry R . Although we consider full continuous rotation symmetry, discrete rotation symmetry C_n with $n > 2$ is sufficient in restricting the form of the effective $k \cdot p$ theory up to $O(k^3)$. We take their action in the spin/orbital subspace to be the following

$$P = \sigma_x \otimes I \quad T = I \otimes i s_y K \quad R_\theta = I \otimes \exp\left(i \frac{\theta}{2} s_z\right) \quad (\text{B1})$$

In addition, P sends $k \rightarrow -k$, T sends k to $-k$, and R_θ sends $\vec{k} \rightarrow \mathbf{R}_\theta \vec{k}$ when acting on Bloch states, where \mathbf{R}_θ is the rotation matrix by angle θ . By requiring PT to be a symmetry of the Hamiltonian, among the 16 possible choices

$\sigma_\alpha \otimes s_\beta$ $\alpha, \beta = 0, 1, 2, 3$, only the following are permissible (commutes with PT)

$$\begin{aligned} \sigma_z \otimes s_{\beta=1,2,3} & p = -1 \quad t = -1 \\ \sigma_x \otimes I & p = 1 \quad t = 1 \\ \sigma_y \otimes I & p = -1 \quad t = -1 \\ I \otimes I & p = 1 \quad t = 1 \end{aligned} \quad (\text{B2})$$

The $p, t = \pm 1$ after each line indicates whether that operator commutes with P ($p = 1$) or anticommutes with P ($p = -1$). $I \otimes I$ is trivial, so we will ignore it from now on. Then when doing $k \cdot p$ expansion of the Hamiltonian, the most general form is the following (ignoring the constant term, and up to k^2 term)

$$H(k) = H_x k_x + H_y k_y + H_{xx} k_x^2 + H_{yy} k_y^2 + H_{xy} k_x k_y \quad (\text{B3})$$

$$H = \sum_k (a_{k\uparrow}^\dagger, b_{k\uparrow}^\dagger, a_{k\downarrow}^\dagger, b_{k\downarrow}^\dagger) H(k) (a_{k\uparrow}, b_{k\uparrow}, a_{k\downarrow}, b_{k\downarrow})^T \quad (\text{B4})$$

Given that P sends the momentum of the operator from k to $-k$, then H_x and H_y can only be expressed in terms of those matrices with $p = -1$. Similarly, H_{xx}, H_{yy}, H_{xy} can only be expressed in terms of those matrices with $p = 1$. Without further invoking rotation symmetry, this is as far as we can go for constructing the Hamiltonian.

Let us first work with the k^2 order terms. We have argued that the Hamiltonian must of the following form

$$H_2(k) = (C + Dk_x^2 + Ek_y^2 + Fk_x k_y) \sigma_x \otimes I \quad (\text{B5})$$

Since R acts trivially in the orbital subspace, and $\sigma_x \otimes I$ is trivial in the spin subspace, rotational symmetry requires

$$Dk_x^2 + Ek_y^2 + Fk_x k_y = Dq_x^2 + Eq_y^2 + Fq_x q_y \quad (\text{B6})$$

where $\vec{q} = \mathbf{R}_\theta \vec{k}$. This then tells us that $D = E, F = 0$. (From the proof here, it is clear that continuous rotational symmetry is not necessary, any discrete rotational symmetry C_n for $n \geq 3$ is sufficient)

We then proceed to the linear terms. Here H_x, H_y can only be written in terms of linear combinations of $\sigma_z \otimes s_\beta = 1, 2, 3$ and $\sigma_y \otimes I$. Notice that $\sigma_y \otimes I$ commutes with rotation operator R . Then rotational symmetry forbids the presence of $\sigma_y \otimes I$. By forbidding, we mean the following. Assume that we write the following Hamiltonian

$$H_{\text{assume}} = \sum_k (a_{k\uparrow}^\dagger, b_{k\uparrow}^\dagger, a_{k\downarrow}^\dagger, b_{k\downarrow}^\dagger) (c_1 k_x + c_2 k_y) \sigma_y \otimes I (a_{k\uparrow}, b_{k\uparrow}, a_{k\downarrow}, b_{k\downarrow})^\dagger \quad (\text{B7})$$

By requiring $RH_{\text{assume}}R^{-1} = H_{\text{assume}}$, we arrive at the conclusion $c_1 = c_2 = 0$. By the same reasoning $\sigma_z \otimes s_z$ is also forbidden.

Then we are only left with the possibility of $\sigma_z \otimes s_{x,y}$. By essentially the same reasoning we had when dealing with H_{assume} , we find that the linear term must be of the following form [107]

$$H_1(k) = (k_x \sigma_z s_x + k_y \sigma_z s_y) \quad (\text{B8})$$

Then putting together our Hamiltonian $H_1(k)$ and $H_2(k)$, we find that the most general Hamiltonian consistent with all the symmetry is the following

$$H(k) = A(k_x \sigma_z \otimes s_x + k_y \sigma_z \otimes s_y) + (C + Dk^2) \sigma_x \otimes I \quad (\text{B9})$$

Let us define a new set of Pauli matrices τ and μ in the following manner

$$\tau_z = \sigma_x s_z \quad \mu_z = \sigma_x \quad \mu_x = \sigma_y s_y \quad \mu_y = \sigma_z s_y \quad (\text{B10})$$

Notice that μ anticommutes within themselves and all three μ commutes with τ . In terms of the newly defined Pauli matrices, the Hamiltonian can be written as

$$H = A(\tau_z \mu_x k_x + k_y \mu_y) + (C + Dk^2) \mu_z \quad (\text{B11})$$

This is exactly the form of the Hamiltonian we presented in the main text. As a matter of fact, there are lots of degrees of freedom when defining the μ and τ . For example, we could have also defined it in the following manner

$$\mu_x = \sigma_z \otimes s_x \quad \mu_y = -\sigma_y \otimes s_x \quad \mu_z = \sigma_x \otimes I \quad \tau_z = \sigma_x \otimes s_z \quad (\text{B12})$$

Then $H(k)$ will be slightly different in terms of τ and μ , but the physics is invariant. Finally, a term proportional to $(k_x^2 + k_y^2) I \otimes I$ is always allowed, which will lead to a particle-hole mass asymmetry ($\alpha_1 \neq \alpha_2$ in the main text).

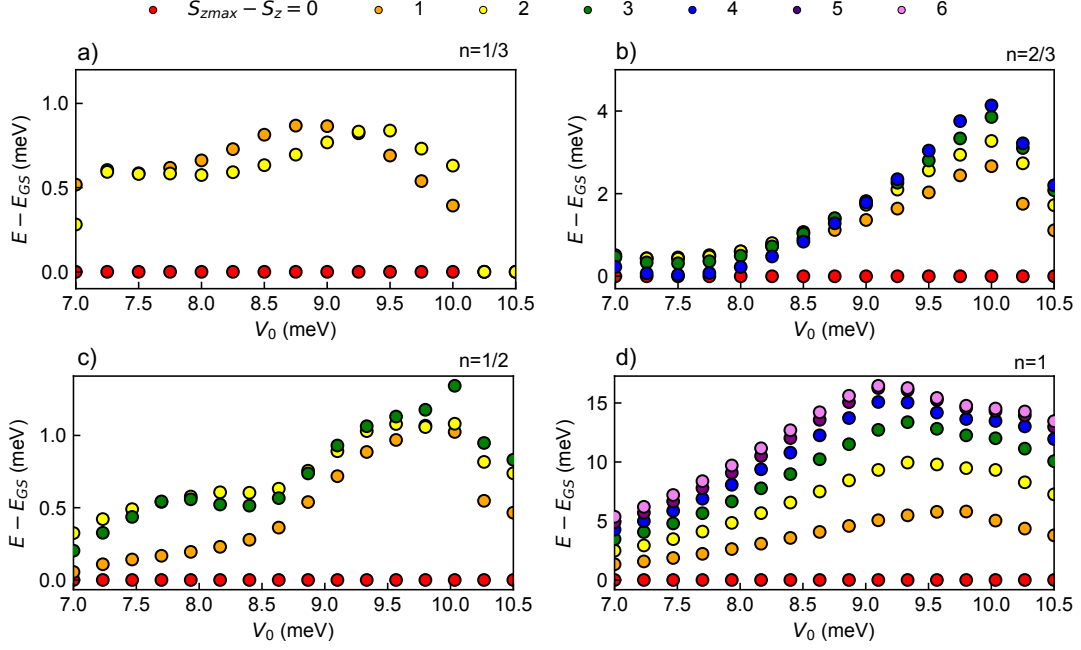


FIG. S5. Magnetism of Cd_3As_2 from numerical diagonalization. Lowest energy level within each S_z eigensector as a function of superlattice potential strength V_0 at $n = \frac{1}{3}$ (a), $\frac{2}{3}$ (b), and $\frac{1}{2}$ (c), and 1 (d) hole filling of the first Cd_3As_2 valence band, demonstrating full S_z polarization within a range of potential strengths. The finite system used contains 12 superlattice unit cells (same as defined in the Supplementary Material of Ref. [62]). Physical parameters are same as in Fig. 4 of the main text.

Appendix C: Many Body Calculation Extended data

Here, we study many-body physics in the first valence band of Cd_3As_2 and expand on the results presented in Fig. 4 of the main text.

In Fig. S5, we show that full S_z polarization occurs at all filling factors studied in Fig. (4) of the main text (Fig. S5). Also, we show many-body spectra at $n = \frac{1}{3}, \frac{2}{3}$ within the fully spin-polarized sector to confirm the ground states' FCI nature (Fig. S6).

In Fig. S6, we show example many-body spectra at $n = \frac{1}{3}, \frac{2}{3}$ to demonstrate the appearance of fractional Chern insulator ground states. We note that fact that the center-of-mass momentum quantum numbers ($k_1 + N_1 k_2$) of the ground states are all the same is inconsistent spontaneous translation symmetry breaking, ruling out the possibility of spontaneous translation symmetry breaking. In Fig. S7, we show similar evidence for FCIs in the first conduction miniband of Sb_2Te_3 (parameters derived in Sec E).

In Fig. S8, we provide evidence for an anomalous composite Fermi liquid at $n = \frac{1}{2}$. Fig. S8 (a) shows that in each of the three momentum sectors $k_1 + N_1 k_2 = 7, 14, 21$ (which are the m points of the mini Brillouin zone), there are two low-lying quasi-degenerate “ground states”. These ground states' center-of-mass momenta obey a “compact composite Fermi sea” rule established in previous numerical studies of composite Fermi liquids [53, 95–99] and are identical to those obtained through numerical diagonalization of the lowest Landau level on an identical system geometry [60]. Fig. S8(b) shows the corresponding momentum distribution function ($n(\mathbf{k}) = \frac{1}{N_{GS}} \sum_i \langle \Psi_i | c_{\mathbf{k}}^\dagger c_{\mathbf{k}} | \Psi_i \rangle$ where i runs over the N_{GS} ground states), which lacks the Fermi surface discontinuity characteristic of Landau Fermi liquid. This numerical evidence indicates an anomalous (zero-field) composite Fermi liquid state at $n = \frac{1}{2}$ [78, 79, 100].

For a detailed discussion of our methods, we refer the reader to the Supplementary Material of Ref. [62].

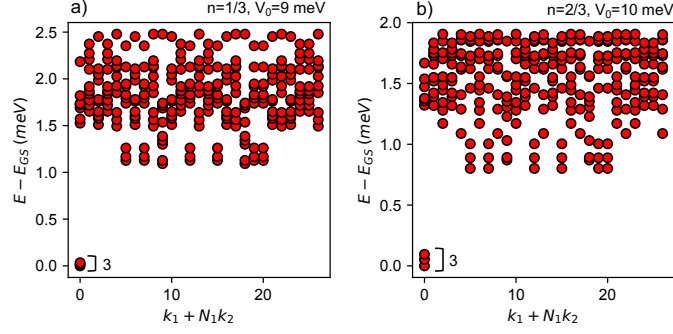


FIG. S6. Evidence of FCIs in Cd_3As_2 . Many-body spectra within maximum S_z sector at and $n = \frac{1}{3}$ (a) and $n = \frac{2}{3}$ (b) hole filling of the first Cd_3As_2 valence miniband, demonstrating gapped, three-fold quasidegenerate FCI ground states. All model parameters are the same as stated in Fig. (4) of the main text. The finite system used contains 27 superlattice unit cells (same as defined in the Supplementary Material of Ref. [62])

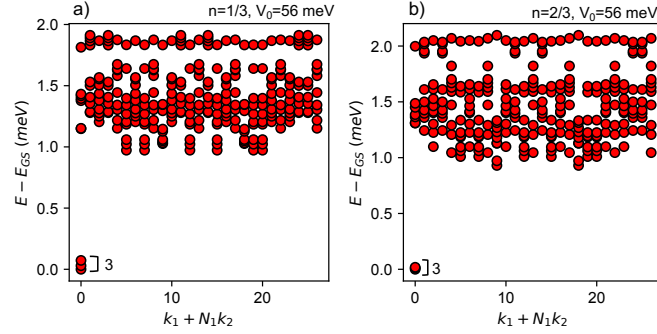


FIG. S7. Evidence of FCIs in Sb_2Te_3 . Analogous to Fig. S6 except for the first conduction miniband of Sb_2Te_3 with layer thickness $L = 2.5\text{nm}$. Parameters entering Eq. 1 of the main text are $\delta = 200.76\text{meV}$, $v = 337.86\text{meV nm}$, $\alpha_1 = 374.6\text{meV nm}^2$, and $\alpha_2 = 567.0\text{meV nm}^2$. The superlattice potential parameters are $V_0 = 56\text{meV}$, $\phi = \pi$, $a = 21\text{nm}$. $\epsilon = 10$.

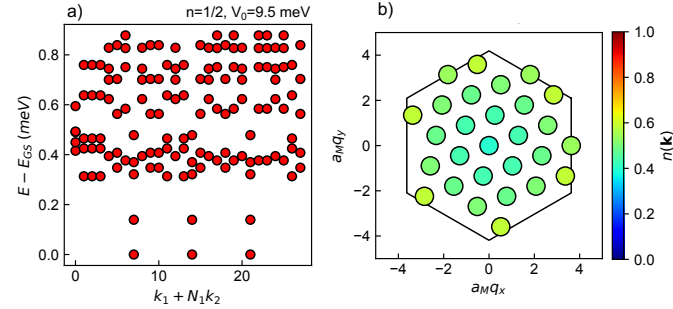


FIG. S8. Evidence of anomalous composite Fermi liquid in Cd_3As_2 . (a) Many-body spectrum within maximum S_z sector at and $n = \frac{1}{2}$. (b) Corresponding momentum distribution function $n(\mathbf{k})$. Physical parameters are the same as in Fig. 4 of the main text.

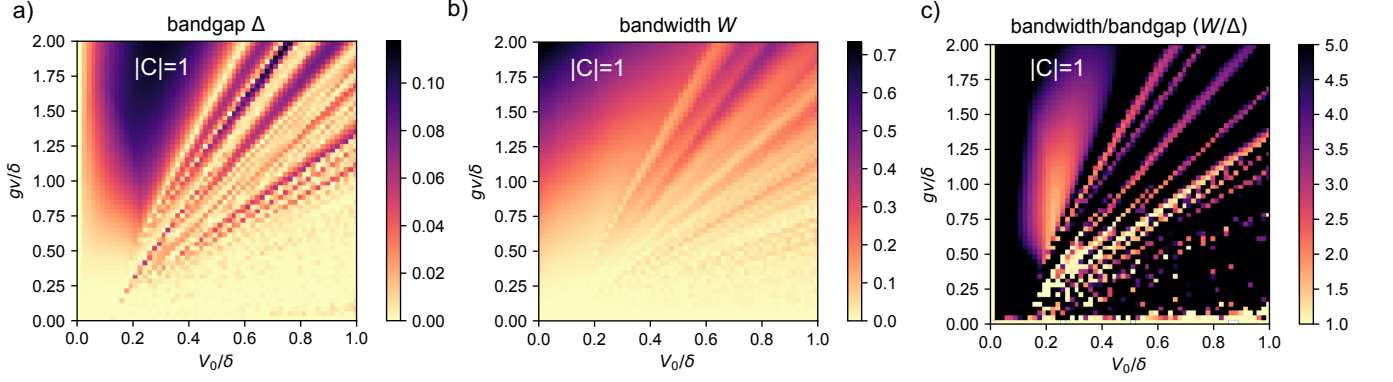


FIG. S9. Bandgap and bandwidth of the massive Dirac fermion model in a periodic potential. (a) Minimum bandgap isolating the lowest conduction band, (b) lowest conduction bandwidth, and (c) their ratio as a function of the two dimensionless parameters characterizing the massive Dirac model given fixed $\phi = 0$.

Appendix D: Massive Dirac model

Here, we discuss on topological minibands in the massive Dirac model with a triangular Bravais lattice periodic scalar potential,

$$H_0^r(\mathbf{k}) = v(\tau k_x \sigma_x + k_y \sigma_y) + \frac{\delta}{2} \sigma_z + V(\mathbf{r}) \quad (\text{D1})$$

where

$$V(\mathbf{r}) = 2V_0 \sum_{n=1}^3 \cos(\mathbf{g}_n \cdot \mathbf{r} + \phi) \quad (\text{D2})$$

as in Eq. (2) in the main text. We find that the model fails to exhibit topological minibands with small bandwidth-to-bandgap ratios. We also find that it is unlikely to exhibit integer or fractional quantized anomalous Hall effects at the filling $n \leq 1$, where n is the number of carriers per superlattice unit cell.

This model has been studied previously in Ref. [47, 48]. It was shown that topological bands occur in the conduction band when the phase parameter $\phi \bmod \frac{2\pi}{3} \sim 0$, corresponding to a potential with honeycomb minima. This result can be understood by calculating the C_3 eigenvalues at C_3 -symmetric points of the mini-Brillouin zone, which fix the Chern number mod 3 [101], via degenerate perturbation theory in the weak superlattice potential limit. This model is characterized, up to an overall energy scale, by the dimensionless parameters gv/δ and V_0/δ , and ϕ where $g = |\mathbf{g}_1|$.

While a superlattice potential with $\phi = 0^\circ$ produces a topological conduction miniband, we find numerically that the ratio its bandwidth to the gap separating it from the next conduction miniband cannot be made small (Fig. S9). We interpret this result as follows. In the limit $\delta \rightarrow \infty$, the Hamiltonian reduces to a standard \mathbf{p}^2 kinetic energy Hamiltonian with a periodic potential. The lowest two minibands have honeycomb lattice character with gapless mini-Dirac points at κ, κ' . As δ decreases from ∞ , these mini Dirac points gap out, resulting in a $|C| = 1$ lowest conduction miniband.

On the other hand, the miniband spectrum of the massless ($\delta = 0$) Dirac model is gapless. In particular, when $\delta = 0$, there are mini-Dirac points between the lowest two conduction minibands each of the three inequivalent mini-Brillouin zone edge midpoints, m, m', m'' . [102, 103]. One can show that the presence of a pseudo-time reversal symmetry ($\tilde{T} = -i\sigma_y \mathcal{K}$, $[\tilde{T}, H] = 0$) when $\delta = 0$ guarantees double degeneracies for a fixed τ at all crystal momenta \mathbf{k} invariant under $\mathbf{k} \rightarrow -\mathbf{k}$ (that is, γ and m points). Here \mathcal{K} is the complex conjugation operator and we emphasize the prefix ‘‘pseudo’’ since we have not specified the physical meaning of σ . The size of the direct gaps at κ, κ' and m, m', m'' behave oppositely with δ , the bandgap resists becoming large as δ is tuned (see Fig. S9 (a-d)).

In Fig. S9, we show the small direct bandgap Δ , bandwidth W , and their ratio for the lowest conduction minibands as a function of the two dimensionless parameters gv/δ and V_0/δ with fixed $\phi = 0$. While we observe a large region of parameter space in which $|C| = 1$, the bandwidth-to-bandgap ratio in this regime does not become small, achieving a minimum value near ~ 1.4 .

We now examine the possibility of an integer quantized anomalous Hall state by performing exact diagonalization calculations in Fig S10. One might expect that, given sufficiently strong interactions, a calculation projected only to

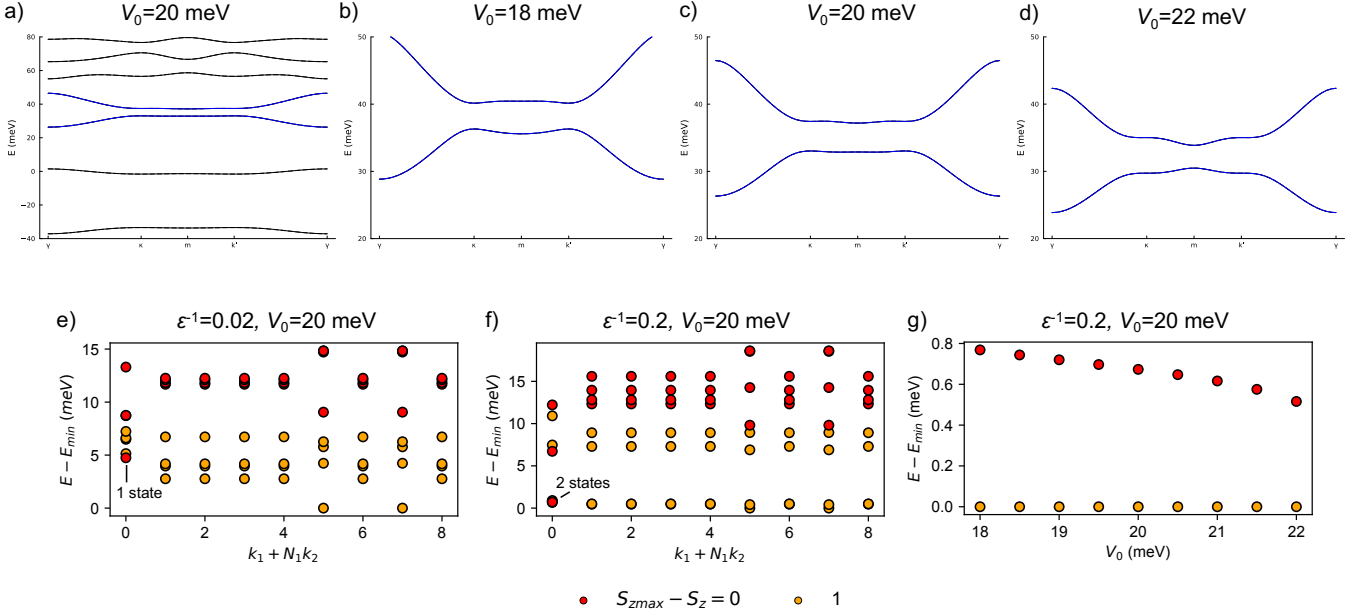


FIG. S10. Absence of QAH in the massive Dirac fermion model from two-band numerical diagonalization. (a-d) Example band structures of lowest two conduction minibands corresponding to the $|C| = 1$ region of Fig. S9(d) where the bandwidth/bandgap ratio is maximized. (e-g) Many-body calculations demonstrating absence of IQAH state (see text). Parameters: $\delta = 90$ meV, $v = 200$ meV nm, $a_M = 20$ nm, $\phi = 0^\circ$, corresponding to $V_0/\delta = 0.22$, $gv/\delta = 0.81$.

the lowest conduction miniband in each valley would indeed give a τ -polarized IQAH groundstate, and this is indeed what we observe (not shown). However, the small value of the bandgap brings the reliability of such a calculation into question. We thus expand our Hilbert space to also include the second lowest conduction miniband within each τ sector and find that IQAH state never becomes the ground state. Due to Hilbert space dimension limitations, we compare only the S_{zmax} and $S_{zmax} - 1$ sectors (see main text). In the absence of interactions, the unique lowest energy state within the maximally τ polarized sector is the full-band Chern insulator state. However, a finite bandwidth means that a non-valley polarized Fermi liquid state is lower in energy. As we increase interactions, we observe a level crossing within the maximally τ -polarized sector *before* we observe full τ polarization. After the level crossing, there are two nearly degenerate low-energy states within the S_{zmax} sector. These two energy states likely correspond in the thermodynamic limits to topologically trivial insulating states in which charge polarized to one sublattice of the honeycomb lattice of superlattice potential minima. Exact diagonalization calculations at fractional filling, assuming S_z polarization and projecting only to the lowest band, also fail to exhibit evidence of fractional quantum anomalous Hall states (not shown).

Appendix E: Real Materials

In this section, we discuss the procedure for modeling real material candidates for the mechanism presented in the main text.

1. From 3D bulk Hamiltonian to 2D thin film

The starting point is the low-energy 3D Hamiltonian [104, 105]

$$H(\mathbf{k}) = (C + D_1 k_z^2 + D_2(k_x^2 + k_y^2)) + (M - B_1 k_z^2 - B_2(k_x^2 + k_y^2))\sigma_z + A_1 k_z \tau_z \sigma_x + A_2(k_x \tau_x \sigma_x + k_y \tau_y \sigma_x) \quad (\text{E1})$$

We consider Cd_3As_2 (shown in the main text) and Sb_2Te_3 (not shown in the main text). We use parameters for Sb_2Te_3 from Ref.[105], and parameters for Cd_3As_2 from Ref.[106]. For completeness, we reproduce them here. For

Cd₃As₂,

$$\begin{aligned} M_1 &= 0.0205\text{eV} & A_1 &= 0.0\text{eV}\text{\AA} & A_2 &= 0.889\text{eV}\text{\AA} & B_1 &= 18.77\text{eV}\text{\AA}^2 \\ B_2 &= 13.5\text{eV}\text{\AA}^2 & C &= -0.0145\text{eV} & D_1 &= 10.59\text{eV}\text{\AA}^2 & D_2 &= 11.5\text{eV}\text{\AA}^2 \end{aligned} \quad (\text{E2})$$

and for Sb₂Te₃,

$$\begin{aligned} M_1 &= -0.22\text{eV} & A_1 &= 0.84\text{eV}\text{\AA} & A_2 &= 3.4\text{eV}\text{\AA} & B_1 &= -19.64\text{eV}\text{\AA}^2 \\ B_2 &= -48.51\text{eV}\text{\AA}^2 & C &= 0.001\text{eV} & D_1 &= -12.39\text{eV}\text{\AA}^2 & D_2 &= -10.78\text{eV}\text{\AA}^2 \end{aligned} \quad (\text{E3})$$

To construct low energy Hamiltonian for the thin film, we substitute k_z by $-i\partial_z$ in $H(\mathbf{k})$. For film of thickness L , we choose basis states along the z direction as

$$|n_z, \tau_z, \sigma_z\rangle = \sqrt{\frac{2}{L}} \sin\left(\frac{n_z\pi}{L}z\right) \quad (\text{E4})$$

where $n_z = 1, 2, \dots$ are positive integers, and L is the thickness of the film. Then, the Hamiltonian can be constructed by computing the matrix elements of $H(k_x, k_y, k_z \rightarrow -i\partial_z)$ in the basis of $|n_z, \tau_z, \sigma_z\rangle$, and the eigenstates for any (k_x, k_y) can be obtained. We notice that there is an isospin symmetry $I_1 \equiv \tau_z \sigma_z (-1)^n$ such that $H(k_x, k_y, k_z \rightarrow -i\partial_z)$ does not mix between different isospin sectors. Note that for Cd₃As₂, there is an higher symmetry and $I_2 = \tau_z \sigma_z$ is also a conserved isospin. For the remainder of this section, we focus on the $I_1 = -1$ sector for Sb₂Te₃ and $I_2 = -1$ sector for Cd₃As₂ (note that this choice of I_2 or I_1 for Cd₃As₂ makes no difference here, but will be useful in Sec E 3 b).

Fig S11 shows the energy of the valence and conduction bands as a function of film thickness L for these two materials. Since $H(0, 0, -i\partial_z)$ commutes with τ_z , these states can be labeled by their τ_z eigenvalue. Based on the criterion discussed in the main text, we choose thicknesses $L = 2.5$ nm for Sb₂Te₃ and $L = 8$ nm for Cd₃As₂. For this choice of L , the conduction and valence bands have opposite τ_z eigenvalue.

To obtain the two-band model of the thin film, used in the main text, we do a further $k \cdot p$ expansion of this Hamiltonian. Specifically, let $|1\rangle$ and $|2\rangle$ be the two states closest to charge neutrality in the $I_1 = -1$ sectors of $H(0, 0, -i\partial_z)$ with energies E_1 and E_2 . In terms of these two states, we may define the following 2-by-2 matrices,

$$\begin{aligned} (H_0)_{i,j} &= \langle i | H(0, 0, -i\partial_z) | j \rangle \\ (H_x)_{i,j} &= \langle i | \partial_{k_x} H(0, 0, -i\partial_z) | j \rangle \\ (H_y)_{i,j} &= \langle i | \partial_{k_y} H(0, 0, -i\partial_z) | j \rangle \\ (H_{xx})_{i,j} &= \langle i | \partial_{k_x}^2 H(0, 0, -i\partial_z) | j \rangle \\ (H_{yy})_{i,j} &= \langle i | \partial_{k_y}^2 H(0, 0, -i\partial_z) | j \rangle \end{aligned} \quad (\text{E5})$$

where

$$\begin{aligned} H(0, 0, -i\partial_z) &= C - D_1 \partial_z^2 + (M + B_1 \partial_z^2) \sigma_z - iA_1 \partial_z \tau_z \sigma_x \\ \partial_{k_x} H(0, 0, -i\partial_z) &= A_2 \tau_x \sigma_x \\ \partial_{k_y} H(0, 0, -i\partial_z) &= A_2 \tau_y \sigma_x \\ \partial_{k_x}^2 H(0, 0, -i\partial_z) &= D_2 - 2B_2 \sigma_z \\ \partial_{k_y}^2 H(0, 0, -i\partial_z) &= D_2 - 2B_2 \sigma_z \end{aligned} \quad (\text{E6})$$

Then, the two-band thin film Hamiltonian, given by a Taylor expansion near $\mathbf{k} = 0$, is

$$h_{\text{thin-film}}(k_x, k_y) = H_0 + H_x k_x + H_y k_y + H_{xx} \frac{k_x^2}{2} + H_{yy} \frac{k_y^2}{2} \quad (\text{E7})$$

The fact that $|1\rangle$ and $|2\rangle$ have opposite τ_z eigenvalues implies that H_{xx} and H_{yy} will be diagonal, H_x and H_y will be off-diagonal. Thus, $h_{\text{thin-film}}$ will be exactly the form of the Hamiltonian describing topological band inversion, as used in the main text.

For the Hamiltonian in the main text Eq.1, the parameters we obtain are: for Cd₃As₂,

$$\delta = 16.9 \text{ meV}, \quad v = 88.9 \text{ meVnm}, \quad \alpha_1 = 250 \text{ meVnm}^2, \quad \alpha_2 = 20 \text{ meVnm}^2 \quad (\text{E8})$$

and for Sb₂Te₃,

$$\delta = 200.76 \text{ meV}, \quad v = 337.86 \text{ meVnm}, \quad \alpha_1 = 374.6 \text{ meVnm}^2, \quad \alpha_2 = 567.0 \text{ meVnm}^2 \quad (\text{E9})$$

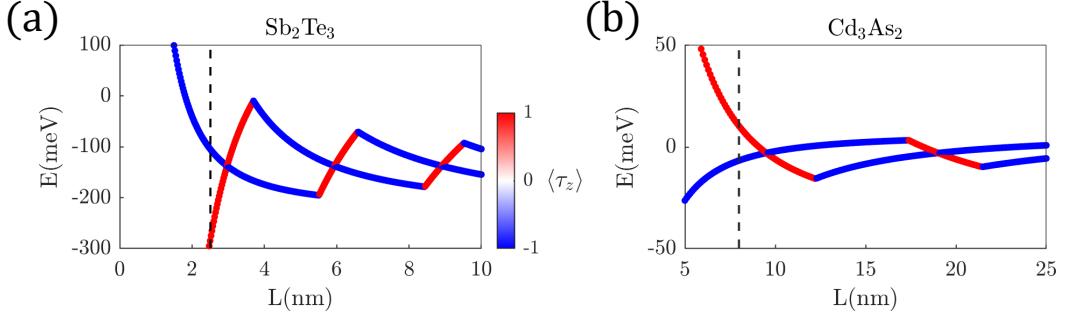


FIG. S11. Energy and τ_z eigenvalues of the two eigenstates of $H(k_x = 0, k_y = 0, k_z \rightarrow -i\partial_z)$ that are closest to charge neutrality. (a) for Sb_2Te_3 thin film in $I_1 = -1$ sector, (b) for Cd_3As_2 thin film in $I_2 = -1$ sector. E is the energy of the state, L is the thickness of the thin film. The dashed line is the thickness we use for all our single particle and ED calculation. The difference in E of the two states is the parent gap.

2. Sb_2Te_3

The properties of Cd_3As_2 are discussed at length in the main text. Here, to show that Cd_3As_2 is not a special case, we also show results for another material candidate Sb_2Te_3 .

The properties of the resulting first conduction (valence) minibands of Sb_2Te_3 at $L = 2.5$ nm, in the presence of a triangular (honeycomb) potential, are shown in Fig.S12(c-f) for a superlattice period $a = 21$ nm. As expected from our results in the main text, a dip in the bandwidth and corresponding quantum geometric indicators is observed at $V_0 \sim 55$ meV as we scan through V_0 . This indicates that the band has become most ideal for hosting fractionalized state near this point. The minibands at this dip are shown in Fig.S12 (b) for the triangular lattice potential.

3. Cd_3As_2 and influence of the thickness of the thin film

Here, we show further extended data on Cd_3As_2 thin film, beyond what is shown in the main text.

a. Other superlattice potential periods

In the main text, we showed the data for Cd_3As_2 when the potential period is $a = 20$ nm. Here, we demonstrate that this is not a fine-tuned result, and that a similarly flat band also emerges for a wide range of superlattice periods. Fig. S13 shows the properties of the first valence band for a superlattice potential $a = 5$ nm and $a = 10$ nm. Both of these show a pronounced dip in the bandwidth and quantum geometric properties, similar to that observed for $a = 20$ nm used in the main text.

b. Finite thickness of the film

In the main text, we model the effect of the electrostatic potential as a scalar potential that couples only to the total in-plane density. However, when the potential arises from a 2D substrate on one side[29], it will decay exponentially in the z direction as $\exp(-Gz)$, where G is the length of the primitive reciprocal lattice vector of the potential, and z is the distance from the substrate. If the film thickness is small so $GL \ll 1$, then it is a reasonable approximation to ignore this z -dependence. However, we chose $L = 8$ nm as the thickness for Cd_3As_2 , while the potential period is $a = 20$ nm. It may therefore be important to take this effect into account.

Without considering the z -dependence, the C_3 symmetric scalar potential is

$$V(\mathbf{r}) = 2V_0\sigma_0 \sum_{n=1}^3 \cos(\mathbf{g}_n \cdot \mathbf{r} + \phi) \quad (\text{E10})$$

where σ_0 acts on the orbital space of the Hamiltonian describing the topological band inversion, as defined in the main text. When the z -dependence of the potential is taken into account, the $I_1 = \tau_z\sigma_z(-1)^n$ isospin is no longer conserved.

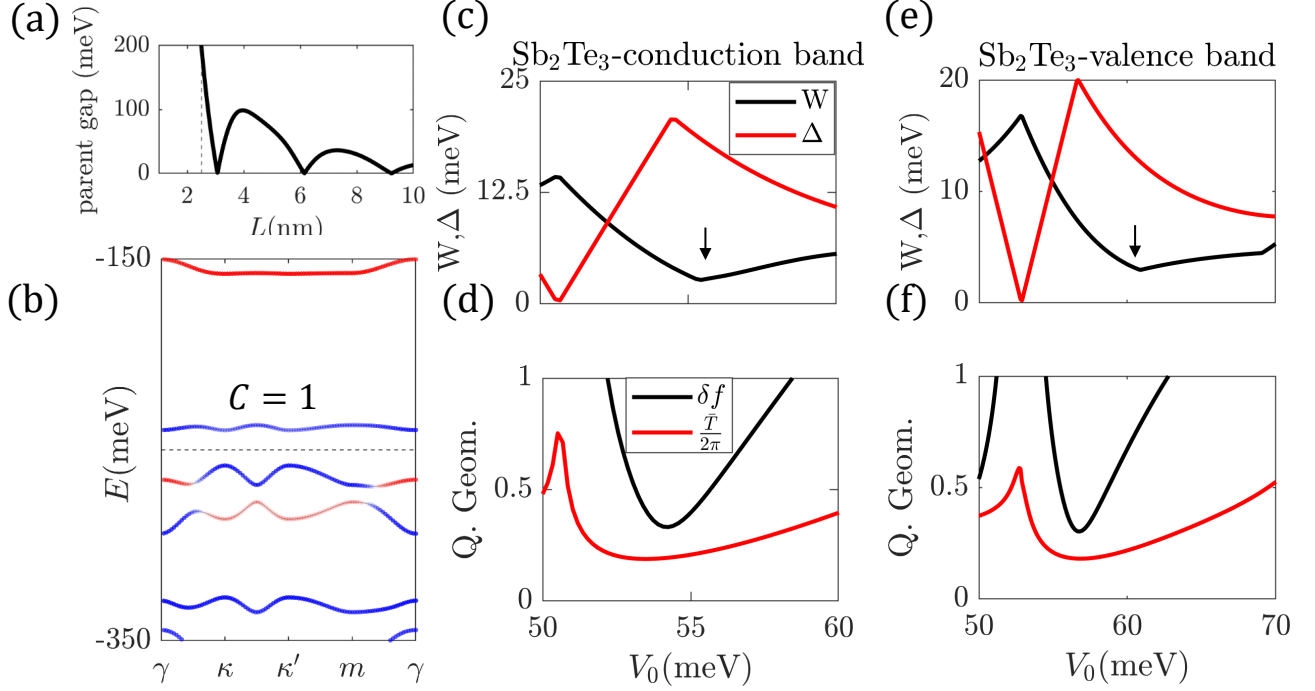


FIG. S12. Electronic and geometric properties of Sb_2Te_3 thin film in a superlattice potential. (a) Gap of the pristine Sb_2Te_3 thin film as a function of film thickness L . The gray dashed line is at $L = 2.5$ nm, which is the thickness we used for (b-f). (b) Minibands with $a = 21$ nm, $V_0 = 55$ meV, $\phi = \pi$. Color of the bands indicates orbital content of the band (cf. main text Fig. 1 and Fig. 3). (c,d) Properties of the first conduction band as a function of V_0 with $\phi = \pi$ and $a = 21$ nm. (e,f) Properties of the first valence band as a function of V_0 with $\phi = 0$ and $a = 21$ nm. The arrow indicates the point where bandwidth/gap, and quantum geometry, is optimized to host fractionalized phases.

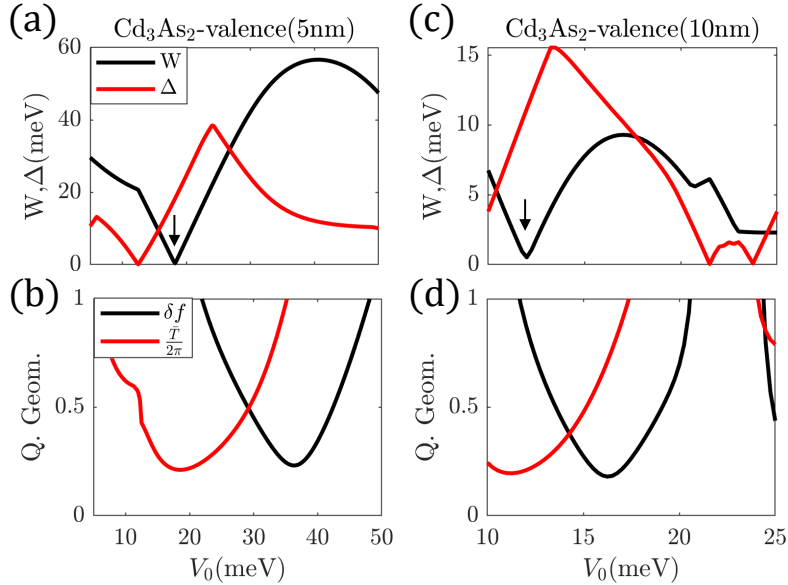


FIG. S13. Properties of the first valence miniband of Cd_3As_2 for various superlattice periods. The bandwidth W , direct gap Δ , Berry curvature standard deviation δf , trace-condition violation \bar{T} , as a function of potential strength V_0 for $\phi = 0$. (a,b) for the potential period $a = 5$ nm, (c,d) for the for $a = 10$ nm. Black arrow indicates the optimal point where bandwidth is minimized.

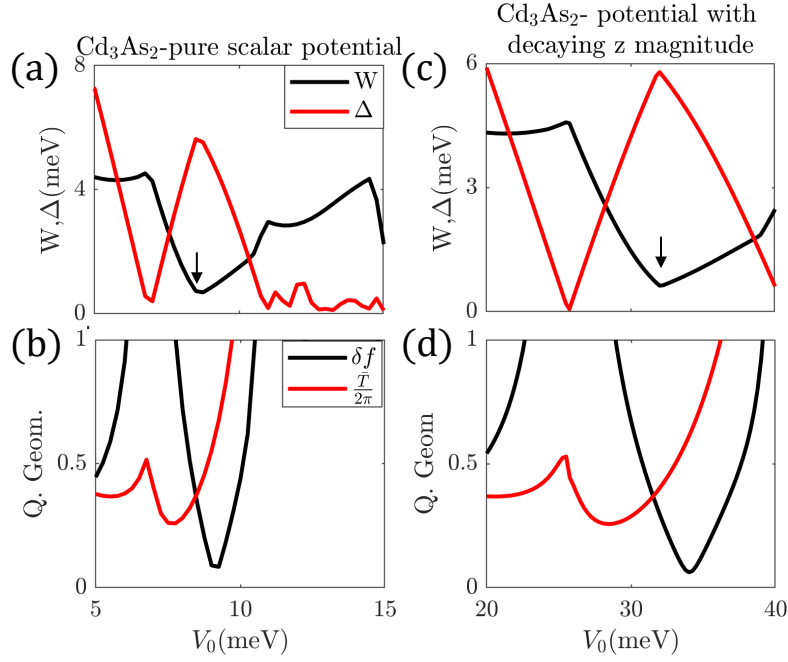


FIG. S14. Taking into account the finite thickness of the Cd_3As_2 film. Parameters used are potential period is $a=20\text{nm}$, potential shape $\phi = 0$. (a,b) ignores the decaying magnitude of the potential along the z direction, while (c,d) takes this decay into consideration by the method specified in the text. Black arrow indicates the point where bandwidth is minimized.

However, the I_2 isospin, defined earlier for Cd_3As_2 , is still a conserved quantum number even in the presence of such a potential. We therefore focus on the $I_2 = -1$ sector for the following.

To model the z dependence of the potential, we define the following 2-by-2 matrix

$$(H_V)_{i,j} \equiv \langle i | \exp(-Gz) | j \rangle \quad (\text{E11})$$

where z should be understood as an operator acting on the original $|n_z, \tau_z, \sigma_z\rangle$ basis (defined in Eq E4), and $|1\rangle, |2\rangle$ are the two eigenstates of $H(k_x = 0, k_y = 0, k_z \rightarrow -i\partial_z)$ closest to charge neutrality in the $I_2 = -1$ sector. We substitute σ_0 by H_V in $V(\mathbf{r})$ to account for the z -dependence.

As we show in Fig. S14, the primary effect of this z -dependence is to shift the position of the dip in bandwidth and quantum geometrical quantities. However, the fact that such a minimum exists is robust. We scan V_0 for both the case with and without considering the effect of the decaying z potential. For pure scalar potential case, the dip occurs at $V_0 \sim 10\text{meV}$. Taking into consideration of the z -decay shifts V_0 to around 30meV .

c. Beyond two-band approximation

In the above, we have presented results when we only project to the two bands closest to charge neutrality. In principle, the number of bands we use when doing the $k \cdot p$ projection should be determined by convergence of the resulting minibands. When the z -dependence is ignored, the results presented above for Cd_3As_2 and Sb_2Te_3 are already well converged in the two-band approximation. However, $\exp(-Gz)$ will have non-negligible elements between the two lowest bands and other remote bands, making it necessary to keep more bands when doing the $k \cdot p$ projection.

Fig.S15 shows the results of keeping more bands when doing the $k \cdot p$ expansion for Cd_3As_2 , including the effect of z -dependence. We find that the dip in bandwidth and quantum geometrical quantities only shifts in position, demonstrating its robustness as expected based on the physical picture of its origin presented in the main text.

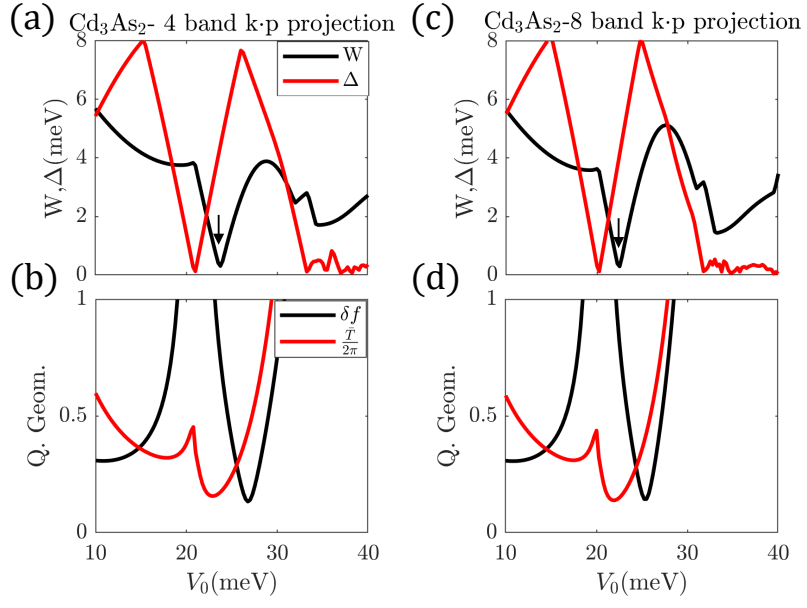


FIG. S15. Same as Fig.S14(c,d), except that we keep more bands in when doing the $k \cdot p$ expansion. (a,b) shows the results for keeping 4 bands, and (c,d) shows the results for 8 bands.